Remote Sensing of Environment 274 (2022) 112950

Contents lists available at ScienceDirect

Remote Sensing of Environment

journal homepage: www.elsevier.com/locate/rse

What lies beneath: Vertical temperature heterogeneity in a Mediterranean woodland savanna

Miriam R. Johnston [a,*], Ana Andreu [b,c], Joseph Verfaillie [b], Dennis Baldocchi [b], Paul R. Moorcroft [a]

[a] Dept. of Organismic and Evolutionary Biology, Harvard University, 26 Oxford St, Cambridge, MA 02138, USA
[b] Dept. of Environmental Science, Policy and Management, University of California, Berkeley, 130 Hilgard Way, Berkeley, CA 94720, USA
[c] IFAPA, Consejeria de Agricultura, Pesca y Desarrollo Rural, Apdo. 3048 ES-14071, Cordoba, Spain

ARTICLE INFO

Editor: Jing M. Chen

Keywords:
Canopy temperature
Vertical gradient
Woodland savanna
ECOSTRESS
Thermal camera

ABSTRACT

As the availability of satellite and airborne thermal infrared remote sensing (TIR-RS) data increases and their spatial, temporal, and spectral resolutions improve, researchers are finding diverse applications for TIR-RS measurements. TIR-RS is now commonly applied in regional- and continental-scale analyses, such as those focused on fire and surface energy balance. However, its application lags in plant physiology and ecology, for which a finer-scale understanding of plant canopy temperatures would be useful to elucidate plant water dynamics, for example. In particular, while methods to disaggregate TIR-RS pixels in horizontal space have advanced, possible vertical stratification of plant canopy temperature and its implications for understanding the correspondence between TIR-RS and finer-scale, field-based thermal measurements (e.g. made with a thermal camera) remain unexplored. Here, we use data from a thermal camera deployed concurrently with the recent ECOSTRESS mission to quantify vertical temperature gradients within tree canopies and temperatures of over- vs. under-story plants in a Mediterranean woodland savanna. We then leverage diverse ancillary data to maximize the geometric comparability of ECOSTRESS and thermal camera measurements, in order to assess the extent to which the two forms of thermal measurements correspond. Specifically, we ask: (1) What are the patterns of intra-canopy and over- vs. under-story vertical temperature in a Mediterranean woodland savanna?, and (2) How can vertically-resolved, but spatially-limited field-based temperature measurements be reconciled with spatially-extensive, but surface-only, temperature measurements of a space-borne remote sensor? We found consistent patterns of vertical thermal heterogeneity both within tree canopies and between ecosystem over- and understories. The daytime difference between the top and bottom thirds of blue oak canopies was, on average, 0.48 ° C – and sometimes several times larger. Notably, canopy tops are cooler, likely associated with the understory grass reaching daytime temperatures often exceeding over-story temperatures by 10° C. Given the consistency of the intra-canopy temperature gradients, we expected the ECOSTRESS sensor would be in better agreement with camera measurements of canopy tops than bulk canopies or canopy bottoms. However, within-canopy gradients were overwhelmed by other sources of disagreement between the measurements, in part associated with upscaling camera measurements across space. Overall, thermal camera and ECOSTRESS measurements were largely in agreement at night (pixel RMSE = 1.1°C), but they were more divergent during times of low (but >0 W/m^2) and high incoming solar radiation (daytime pixel RMSE = 3.5°C).

1. Introduction

Plant temperature is a fundamental driver of vegetation functioning across scales. At a cellular level, all enzymatic reactions are temperature-dependent, including photosynthesis (Farquhar et al., 1980; Farquhar and Sharkey, 1982), respiration (Atkin and Tjoelker, 2003), and metabolism (Michaletz, 2018). Reaction rates typically have thermal optima (e.g. Sage and Kubien, 2007), albeit with some degree of thermal acclimation under changing conditions (Berry and Bjorkman, 1980; Smith and Dukes, 2017; Wang et al., 2020). At the scale of leaves, temperature is a first-order control on internal leaf vapor pressure, thereby influencing transpiration and plant water balance (Raschke,

* Corresponding author.
E-mail address: johnston.miriam@gmail.com (M.R. Johnston).

https://doi.org/10.1016/j.rse.2022.112950
Received 5 March 2021; Received in revised form 1 January 2022; Accepted 5 February 2022
Available online 18 March 2022

1960). Tissues are damaged at extreme temperatures, and physiological processes are irreparably disrupted (Taiz and Zeiger, 2002). In turn, thermally-dependent physiological processes scale up to influence rates of plant growth, mortality and recruitment, ecological interactions among individuals, species geographic distributions, and biosphere-atmosphere fluxes of carbon, water, and energy (Charney et al., 1975; Shukla and Mintz, 1982).

Plant temperature is also a gauge of vegetation functioning. Brown and Escombe (1905) were among the first to suggest that plant temperature was an indicator of water relations. They described a leaf of the same temperature as its surroundings, "surrounded by air which is not fully saturated with aqueous vapor for the temperature," and identified the situation as "manifestly unstable." The temperature of the leaf would fall because "water-vapour [would] diffuse through stomata if these are in any degree open." Stomatal closure, by limiting plants' ability to offload energy via latent heat, increases temperature (all other factors being equal). Therefore, the diverse conditions affecting stomatal conductance often have a thermal signature. These include, for example, elevated CO_2 (Gray et al., 2016), infection (Chaerle et al., 1999), and water deficit (Jackson et al., 1981; Scherrer et al., 2011; Lapidot et al., 2019).

Together, these thermal influences and indicators of vegetation dynamics motivate strong interest in the patterns of plant temperature across space and time. Historically, temperature measurements of natural vegetation have often been spatially and temporally isolated (e.g. based on contact or infrared thermometer measurements; Medina et al., 1978; Wilson et al., 1987; Rey-Sánchez et al., 2016; Slot and Winter, 2017), but recent advances in satellite (Gillespie et al., 1998; Malakar et al., 2018; Hulley and Hook, 2018) and field-based (Aubrecht et al., 2016; Johnston et al., 2021; Still et al., 2021) thermal remote sensing promise to assuage the paucity of thermal data across time (in the case of field instruments) and space (in the case of sensors on satellites). It is now a priority to explore how these proliferating thermal data types may be compared, in the face of challenges associated with their disparate resolutions and geometries. In particular, field measurements can resolve vertical temperature patterns, while satellite measurements are more comprehensive across horizontal space. Acknowledging ongoing development of methods to disaggregate thermal remote sensing pixels across horizontal space (Anderson et al., 2011; Jones and Sirault, 2014; Cubero-Castan et al., 2015; Xue et al., 2020), we focus here on vertical temperature patterns. Are vertical thermal gradients present? If so, what implications do they have for the correspondence of satellite and field-based thermal measurements?

The extent to which plant temperatures vary as a function of position within the canopy is especially relevant in this era of global change and burgeoning environmental measurement. Vertically-stratified temperatures are likely to be important in accounting for recent observations that canopy position influences plants' drought tolerance (McGregor et al., 2020) and climate sensitivity (Rollinson et al., 2020), as well as in providing context for vertical variation of leaf traits (e.g. Ellsworth and Reich, 1993; Griffin et al., 2002; Kafuti et al., 2020). Development of robust methods for scaling leaf-level measurements to canopies, biomes, and ultimately across the globe requires understanding of spatial and temporal heterogeneity in environmental conditions within plant canopies (Jarvis, 1995), of which vertical structure is a key component (Damm et al., 2020; Banerjee and Linn, 2018). Vertically-resolved energy measurements would also support improved interpretation of both new and established integrative measurements of ecosystem function, including solar-induced fluorescence (Marrs et al., 2020; Maguire et al., 2020) and eddy covariance (Baldocchi et al., 2020).

In this research, we combine data from a laterally-looking thermal camera (FLIR A325sc, Johnston et al., 2021), lidar, field measurements, and the ECOSTRESS instrument on the International Space Station (Hulley and Hook, 2018; Fisher et al., 2020) to quantify vertical plant temperature heterogeneity and to assess its implications for comparisons of satellite and ground-measured plant temperature. Specifically, we ask: (1) what are the patterns of intra-canopy and over- vs. under-story vertical temperature in a Mediterranean woodland savanna?, and (2) How can vertically-resolved, but spatially-limited, temperature measurements be reconciled with spatially-extensive, but surface-only, temperature measurements of a space-borne remote sensor?

We hypothesized that (H1a) the upper leaves in tree canopies would be warmer than the lower leaves during the day because of their greater exposure to incoming solar radiation, and (H1b) canopies would be thermally homogeneous at night. Regarding comparisons among ecosystem vegetation components, we hypothesized that (H1c) the low-lying, aerodynamically smooth grass under-story would be consistently warmer than tree leaves, because it is comparatively uncoupled with the atmosphere and was largely senescent (and therefore not transpiring) during the measurement periods. Regarding the implications of vertical temperature gradients for reconciling satellite-based and ground-based thermal remote sensing, we hypothesized that (H2a) ECOSTRESS temperature measurements would be in stronger agreement with top-of-canopy temperature than with bulk canopy temperature, and (H2b) ECOSTRESS and FLIR-based measurements would diverge the most at times of highest thermal heterogeneity (both vertical and horizontal).

2. Methods

2.1. Methods overview

In this paper, we present two major results. First, we quantify vertical thermal gradients in tree canopies and between trees and understory grass using measurements from a FLIR thermal camera (Fig. 1, "Analysis #1"). The key dataset supporting this analysis comprised thermal images collected by a tower-mounted FLIR thermal camera over three dry seasons (when oaks have leaves). We corrected the raw thermal measurements for target emissivity, distance between the target and the sensor, reflected radiation, air temperature, and the effect of the enclosure according to methods detailed in Aubrecht et al. (2016) and Johnston et al. (2021).

Second, we leverage diverse ancillary datasets to maximize the geometric comparability of FLIR and ECOSTRESS measurements, and we assess their correspondence (Fig. 1, "Analysis #2"). Briefly, this entailed using a lidar-based digital surface model, a classified IKONOS image, and sun and sensor geometry to determine the proportion of each vegetation type (oak, pine, shaded grass, and sunlit grass) visible to ECOSTRESS in each pixel. We then use those proportions and FLIR thermal camera measurements of pure vegetation "end-member" temperatures to calculate an expected FLIR-based temperature for each ECOSTRESS pixel.

These two analyses are related by our analysis of the correspondence between FLIR and ECOSTRESS measurements when the FLIR-based thermal map is formulated using top-of-canopy temperatures, vs. when it is formulated using bottom-of-canopy or full-canopy (bulk) temperatures.

2.2. Study area

The study area was a semi-arid woodland savanna in the foothills of the Sierra Nevada Mountains, approximately 60 km southwest of Sacramento (38.432°N, −120.966°W, 177 m elevation). The climate is Mediterranean, with cool, wet winters and hot, dry summers. Air temperature ranges from just below freezing to above 40 °C, with an annual mean of 15.8 °C. Precipitation typically falls only November–May, and averages 559 mm per year. The soils are 1 m deep, silt loam to rocky silt loam, and underlain by fractured metamorphic rock, sedimentary rock, and saprolite.

The over-story is dominated by *Quercus douglasii* (blue oak). There are approximately 290 patchily-distributed blue oak stems per ha, mostly 4.0–9.5 m tall (25th - 75th height percentiles) but reaching a maximum height of 20.8 m. *Pinus sabiniana* (grey pine) are interspersed,

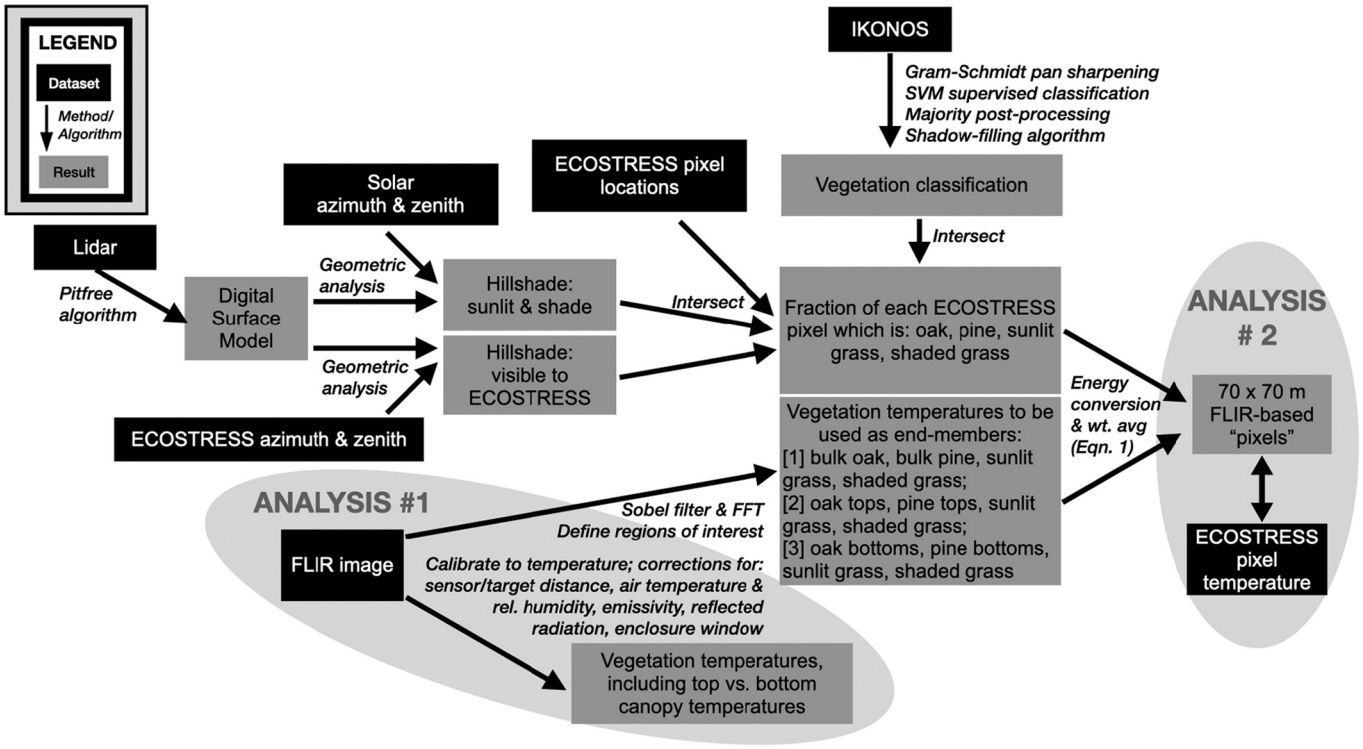

Fig. 1. Summary flowchart of datasets, methods, results, and analyses. Please see text for methods descriptions and results assessments.

with a density of about 50 trees per ha, concentrated in the northeast corner of the approximately 1 × 1 km study area centered on an eddy covariance tower. Most grey pines are relatively small (25th - 75th height percentile is 2.2–6.7 m), but older trees tower over the oaks, reaching a maximum height of 34.0 m. The under-story is a mix of annual C3 grass species that are active during the wet season and senescent in the summer, mostly *Bromus*, *Hypochaeris*, and *Brachypodium*.

Crucially for this research, the trees are sufficiently sparse that a thermal camera mounted 18.0 m high on the eddy covariance tower can image tree canopies at multiple vertical heights and can see through the canopy to the ground. Additionally, as a long-running Ameriflux site (code US-Ton), the area is extensively measured and instrumented. This provides the data required to characterize spatially-explicit structure and composition, to define seasonal dynamics, and to calibrate thermal camera measurements to absolute temperature (Johnston et al., 2021).

2.2.1. Study area vegetation composition

A high-resolution, spatially-explicit vegetation classification map was used to define the proportion of each vegetation component – blue oak, grey pine, sunlit grass, and shaded grass – within 70 × 70-m ECOSTRESS pixels (Fig. 1). We generated this map from an IKONOS satellite image acquired on July 22, 2001 (note that vegetation cover was relatively invariant between the IKONOS acquisition and 2019; see Figs. S1 and S2 for details).

First, we enhanced the spatial resolution of the multispectral IKONOS scene with data from the higher-resolution IKONOS panchromatic band using the Gram-Schmidt Pan Sharpening algorithm (Laben and Brower, 2000; Maurer, 2013). The Gram-Schmidt algorithm is particularly useful in this application of woodland savanna vegetation classification because 4 m multispectral pixels would usually be comprised of multiple vegetation types. Briefly, the lower-resolution multispectral bands are used to simulate a lower-resolution panchromatic image. Then, using this image as the initial vector, a modified Gram-Schmidt vector orthogonalization method is applied to un-correlate the bands. The lower-resolution panchromatic band is replaced with a modification of the higher-resolution original (with gain and bias adjusted according to the orthogonalization), multispectral bands are up-sampled, and the inverse Gram-Schmidt transformation yields the sharpened image (Laben and Brower, 2000; Maurer, 2013). Here, we applied this algorithm using the ENVI image processing and analysis software (Exelis Visual Information Solutions, 2015).

We prepared testing and training data for a classification by randomly selecting 1000 points on the sharpened image to hand-classify into grass, oak, pine, and shadow; we also added approximately 50 extra shadow points and 50 extra pine points to increase sample sizes for those less-prevalent components (see Table S1 for spectral characteristics of the training data). We partitioned the final 1097 hand-classified points into a training set (70% of the points, $n_{grass} = 340$; $n_{oak} = 212$; $n_{pine} = 125$; $n_{shadow} = 91$) and a test set (30% of the points, $n_{grass} = 130$; $n_{oak} = 120$; $n_{pine} = 47$; $n_{shadow} = 32$), and applied a support vector machine supervised classification (SVM). SVM uses statistical learning theory to find an optimal hyperplane in the feature space (in this case characterized by the red, blue, green, and near infrared bands of the pan-sharpened image) that maximizes the separation of the classes (grass, pine, oak, and shadow; Cortes and Vapnik, 1995; Gunn, 1998). We applied a radial basis function kernel to allow the hyperplane to be non-linear in feature space.

To rectify spurious isolated pixels in the resulting classification, we used post-classification majority analyses (3 × 3 window, center pixel weight = 1), which re-classified isolated pixels to match their majority surroundings. To determine how many iterations of majority analysis to apply, we compared the results with the training data; we ran the majority analysis twice. Sharpening, classification, and post-hoc majority analyses were done in ENVI 5.3 (Exelis Visual Information Solutions, 2015); results assessment was done using the "caret" package in R (Kuhn, 2019; R Core Team, 2020).

Finally, to complete the vegetation classification map, we needed to predict vegetation type in the shaded cells, which was impossible using IKONOS data alone. To do this, we applied the following algorithm: (1) assign cells of height < 1 m (according to a canopy height model, see below) to grass; (2) assign cells for which the majority of surrounding cells (within 1 m) were a single vegetation type to that type; (3) in the

case of cells for which no immediately surrounding non-shadow type was in the majority, iteratively extend the neighborhood by one meter and assign the shaded cell the classification of the the plurality surrounding cell vegetation type, once it existed. To assess the efficacy of this algorithm, we tested it on a simulated image comparable to the IKONOS classification, in which the true vegetation cover of the "shaded" pixels the algorithm aimed to assign was known — such that we could compare the cover predicted by the algorithm to the known cover. To create the test image, we sliced the classified IKONOS raster into north-south strips of random width (10–40 1-m pixels) and reshuffled those strips. We then assigned cells on the original classified image which coincided with shadow cells on the simulated image as "unknown," and applied our shadow-filling algorithm to classify them. The purpose of the north/south strips was to maintain a realistic geometry (size, shape, and spatial relationship) of the areas considered unknown/shaded. This is a good measure of accuracy because it provides a test of the algorithm's competency in a context that is highly comparable (very similar geometry of "unknown" areas) to the problem.

The final vegetation classification map had an overall proportion correct classification of 0.84 (95% confidence interval: 0.79, 0.84) and Kappa = 0.76 (Table 1). Except in the case of oak, specificity (proportion of absence correctly identified) was higher than sensitivity (proportion of presence correctly identified) for all cover types. The shadow-filling algorithm had a mean proportion correct classification of 0.78 (sd = 0.012; $n = 15$ reshuffling tests) and a mean Kappa of 0.62 (sd = 0.017). Together, given that 7.7% of the classification was shaded, the expected overall accuracy of the final map is 0.84 (Fig. 2).

2.2.2. Study area digital surface model

A digital surface model (DSM) – capturing both the terrain and the vegetation structure – was required to determine which areas on the ground were visible to the ECOSTRESS sensor (given the sensor's viewing angle) and which were shaded (given solar geometry). We formulated a DSM using a lidar acquisition taken on April 20, 2009. The acquisition had an average posting density of 4.1 points/m^2, a footprint of approximately 18 cm, and a vertical accuracy of -0.01 ± 0.05 m (i.e. lidar-based elevation was, on average, slightly lower than actual elevation). To address errors associated with irregularities in lidar-based height data, which may be associated, for example, with the first lidar return penetrating into the canopy (please see Khosravipour et al., 2014 for additional discussion of "pit" causes), we used the "pitfree" algorithm, as implemented in the lidR package, to calculate the DSM (Roussel and Auty, 2020; Khosravipour et al., 2014). In short, the pitfree algorithm constructs a population of height models: a complete model which uses all lidar first returns, and several partial height models, using only lidar first returns from above specified height values. It combines these into a single height model, which has the maximum model height value at each location (Khosravipour et al., 2014).

Table 1
Vegetation classification confusion matrix and statistics by class. "A" is the prevalence of predicted cover presence in the case of true presence, "B" is the prevalence of false positive predictions, "C" is the prevalence of false negative predictions, and "D" is the prevalence of predicted cover absence in the case of true absence. Bold denotes correct classifications.

		Cover Class			
Prediction		grass	oak	pine	shadow
grass		**102**	5	1	1
oak		27	**109**	7	4
pine		0	6	**37**	0
shadow		1	0	2	**27**
Statistic	**Formula**				
sensitivity (S_1)	A/(A + C)	0.79	0.91	0.79	0.84
specificity (S_2)	D/(B + D)	0.97	0.82	0.98	0.99
balanced accuracy	$(S_1 + S_2)/2$	0.88	0.86	0.88	0.92

Because the lidar acquisition was in 2009, we wanted to ensure that there had not been extensive structural change between 2009 and the thermal measurements. To assess the DSM, we separated it into a digital terrain model (DTM) and a canopy height model (CHM; DSM = DTM + CHM), and we compared the canopy height model to tree heights measured in the field in June 2018. We created the digital terrain model (DTM) using the lidar and a Delauny triangulation-based spatial interpolation, which builds triangles to maximize minimum triangle angles and linearly interpolates within triangles (Roussel and Auty, 2020). We calculated a canopy height model as the difference between the DSM and the DTM. In the comparison of CHM and field data, we omitted under-story trees, defined as individuals located sufficiently close to a taller tree that we expected that they were underneath the neighbor's crown. The definition of "sufficiently close" depended on the size of the neighbor: we used allometric equations developed using field measurements at the site to estimate tree crown widths (Fig. S3). We defined heights of the remaining trees, allowing for minor crown asymmetry, by extracting the maximum CHM value within a 2-m buffer of a surveyed tree trunk location, rather than the CHM height at the exact trunk location.

The correlation between tree heights measured in the field and the lidar-based canopy height model was 0.90. Based on the comparison between the CHM and the field data, we applied a minor linear correction to CHM values >3 m (Fig. S4), which we combined with the DTM to recalculate a corrected DSM. The correction increased very large values of the DSM by up to 4.0 m and decreased small values by up to 1.0 m, but most corrections were minor: the median magnitude of correction was 0.04 m (Q1: 0.00 m, Q3: 0.46 m). The direction of the corrections for taller trees made sense, because lidar typically underestimates tree heights (Disney et al., 2010). Additionally, trees may have grown between the lidar acquisition and the thermal measurements.

2.2.3. Study area leaf-expanded periods

The final characterization of the study area required for this work was a determination of leaf-expanded periods in 2018, 2019, and 2020; it was meaningful to measure leaf temperature with a thermal camera during these time periods only. To define leaf-expanded periods algorithmically, we used gap fraction data from three upward-pointing digital cameras (Ryu et al., 2012). Each camera imaged several branches, and together they collected data representative of the entire site: plant area index calculated using camera data was linearly related to plant area index calculated using spatially-extensive sampling across the site ($R^2 = 0.97$, as described by Ryu et al., 2012. Please see Fig. S5 and its figure legend for details of the algorithm).

Beginning and end dates of the 2018 and 2019 leaf-on periods, and the beginning date of leaf-on in 2020, never varied by greater than six days among the three digital cameras (Fig. S5). The leaf-on period of 2018 was defined as April 24–September 5 (DOY 114–248); the leaf-on period of 2019 was April 23–October 12, (DOY 113–285), and the leaf-on period in 2020 was April 20–July 30 (DOY 111–212). Combined with thermal camera deployment dates, these dates defined analysis times.

2.3. Thermal measurements

2.3.1. Field-based thermal remote sensing: FLIR camera

During the leaf-expanded periods of 2018, 2019, and 2020 (roughly aligning with the dry season at this site), we collected 12,324 half-hourly thermal images with a FLIRA325sc thermal camera: 1036 in 2018 (July 18, 2018 - September 5, 2019), 6495 in 2019 (May 30, 2019 - October 12, 2013), and 4793 in 2020 (April 20, 2020 - July 30, 2020). One-hundred seventy six of these were omitted from further analysis due to precipitation or missing ancillary data required for calibration (see below). The camera was fitted with a lens with 45° field of view, was enclosed in weather-proof housing with a germanium window, and was mounted 18 m above ground level at an inclination angle of −14°,

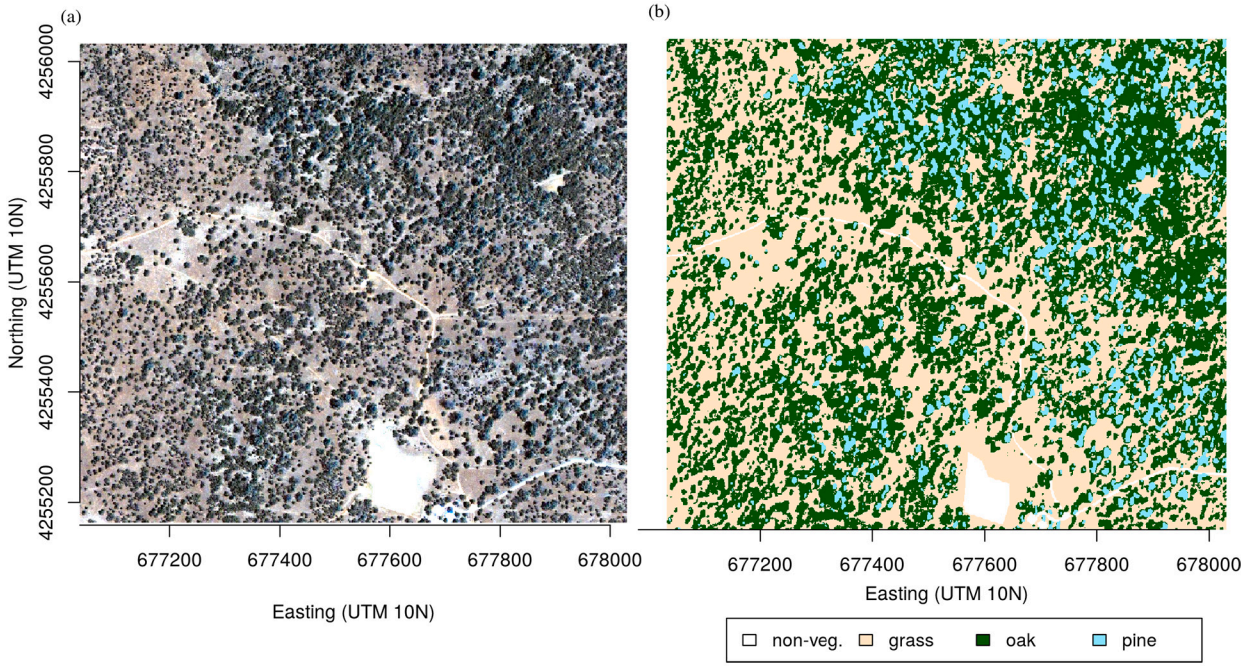

Fig. 2. (a) IKONOS image of the area surrounding the US-Ton flux tower, linearly stretched to enhance the visible difference between pines (more blue, more numerous in the northeast corner) and oaks (darker green). Non-vegetation areas include roads and a seasonal pond in the south. (b) Classified and shadow-filled raster covering the same extent as (a). (For color, the reader is referred to the web version of this article.)

pointing approximately northeast. It had a 240 × 320 pixel resolution, which translates to an on-the-ground resolution ranging from about 6.5 cm (at a 25 m distance from the camera) to about 51.8 cm (at a 200 m distance from the camera). Broadly, the vegetation viewed by the FLIR was representative of the entire 1 × 1 km area around the flux tower (Fig. S6).

In total, we calibrated 24 vegetation regions of interest (ROIs) in the camera's field of view (Fig. 3). We selected ROIs as representative of ecosystem vertical structure and of single canopies as possible, while also minimizing contamination by branches and background pixels. To keep ROIs consistent across the years of measurement, we detected shifts in the camera's field of view using a Sobel filter to find edges within each image and a Fourier fast transform to convolve sequential, filtered images. In the case of shifts, the maximum of the convolution was offset from the center of the image. There were three shifts during our analysis period, and we adjusted ROI locations accordingly. In addition to "bulk" canopy ROIs, as outlined in Fig. 3, we separately considered canopy tops and bottoms, as defined by the top and bottom thirds of ROI pixel rows.

We followed methods detailed in Aubrecht et al. (2016) and Johnston et al. (2021) to correct the raw images for target emissivity, distance between sensor and target, air temperature, air transmissivity, reflected radiation (assumed originating from the sky), and the effects of the enclosure window (please see Table S2 for further details on instrumentation). We calculated transmissivity (0.971) and reflectivity (0.004) of the germanium protective enclosure window (Edmund Optics 8–12 μm anti-reflection coated) using curves provided by Edmund Optics, and we measured window temperature on the internal window surface with a thermocouple. For the 8.5% of images for which we did

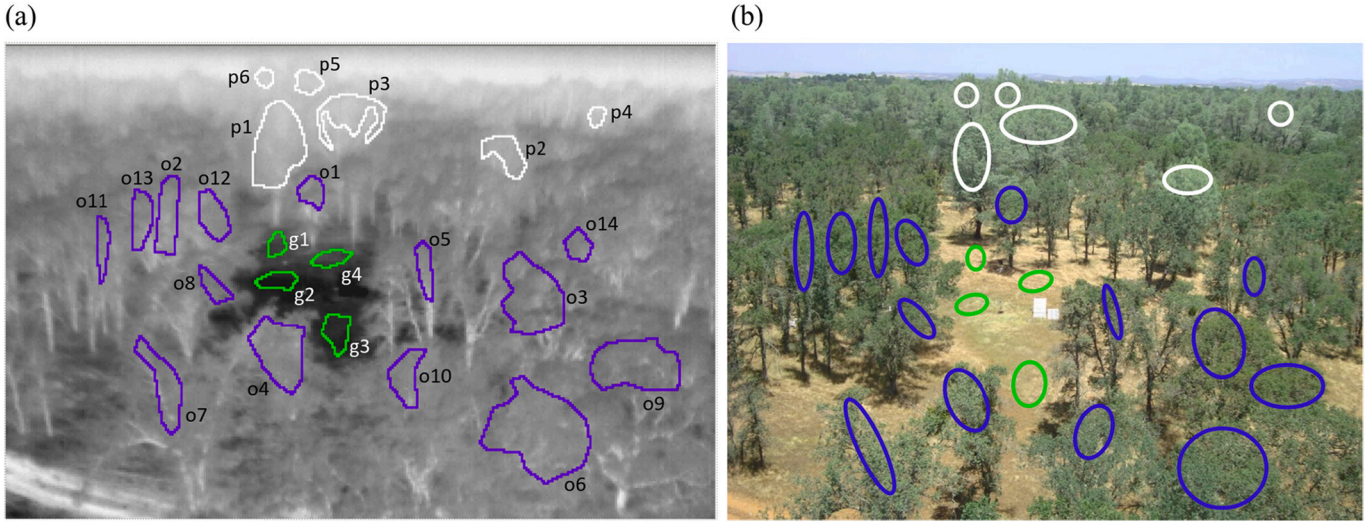

Fig. 3. (a) FLIR A325sc thermal image, with outlined regions of interest (ROIs). Oak ('o') ROIs are blue, pine ('p') ROIs are white, and grass ('g') ROIs are green. (b) Red/green/blue image of the approximate FLIR FOV with approximate ROIs, for context. (For color, the reader is referred to the web version of this article.)

not have window thermocouple readings, we applied a simple linear regression of window temperature as a function of air temperature to predict the missing data (adjusted $R^2 = 0.96$, Fig. S7). We used the two-lid emissivity box method to measure plant tissue emissivities in December 2019 (Rubio et al., 1997, 2003), resulting in the following values: dry grass emissivity = 0.966, oak leaf emissivity = 0.985, and pine leaf emissivity = 0.990 (Johnston et al., 2021). Assuming constant emissivity of vegetation is a simplification because leaf emissivity is variable according to ontogeny (Richardson et al., 2020) and water content (Meerdink et al., 2019). However, we expect that the effect of using constant emissivities in this case is minor, as the grass was largely senescent and the leaves fully expanded during measurement periods. Finally, we assumed that the emissivity of the sky (contributing radiation reflecting off targets) was 1; this is also a simplification (Brutsaert, 1975), but it minimizes errors associated with estimating sky transmissivity (please see Johnston et al., 2021 for further discussion).

The specified accuracy of the FLIR A325sc is ±2 ° C. A comparison of FLIR measurements to two independent temperature measurements of a concrete reference panel, mounted on the ground near the center of the camera's field of view, found that the camera's RMSE across five months of half-hourly imaging (June 1–October 31, 2019) is within this limit, though error associated with individual images may be somewhat larger (particularly at times of high light [Johnston et al., 2021], and see Fig. S8 for FLIR vs. reference panel thermocouple [TC] and infrared thermometer [IRT] comparisons at ECOSTRESS overpass times). We quantified error for each thermal image corresponding with an ECOSTRESS overpass using the reference TC and IRT measurements of the panel. In the case that both the mean TC measurement and the IRT measurement were warmer than the FLIR measurement of the panel, error was positive, with a magnitude equal to the larger of the IRT - FLIR or mean TC - FLIR difference. In the case that both reference measurements were cooler, FLIR error was negative, with a magnitude equal to the larger of the FLIR - IRT or FLIR - mean TC difference. In the case that one reference measurement was warmer and one cooler, we assigned both a positive and a negative error to the FLIR measurements, with magnitudes of the differences between the FLIR and the references. TC and IRT measurements of the reference panel were available only after June 16, 2019. For the eight scenes before this date, we estimated errors based on SW radiation. Three scenes with SW = 0 were assigned error bars with length = mean of measured night-time errors; five scenes with SW > 0 were assigned the error of their nearest SW neighbor (always <25 W/m^2 difference).

2.3.2. Satellite thermal remote sensing: ECOSTRESS

We downloaded all ECOSTRESS Level 2 land surface temperature and emissivity (LST&E) swaths (Hulley and Hook, 2018; Fisher et al., 2020) that corresponded geographically with the 1 × 1 km area centered on the eddy covariance tower and temporally with leaf-expanded conditions and thermal camera images (within 10 min). We included only scenes for which orbit correction had been preformed, and we masked all pixels covered by clouds and which were not considered to have "best quality" LST&E data (Hulley and Freepartner, 2019). We omitted scenes in which >1% of the pixels were masked, to maintain comparability between acquisitions. Fifty-three ECOSTRESS acquisitions, collected at diverse times of day and with view zenith angles 2.9–28.8 degrees (median: 14.9 degrees), met these requirements (Fig. S9). There are several non-vegetated areas near the flux tower, including a narrow dirt road, minimal infrastructure, and a seasonal pond (Fig. 2). ECOSTRESS pixels corresponding with these areas were masked and omitted from subsequent analyses. Error was quantified as the ECOSTRESS-reported land surface temperature accuracy, and assumed to apply in both the positive and negative directions.

2.3.3. Comparing field-based and satellite thermal remote sensing

To compare thermal camera and ECOSTRESS measurements of surface temperature, it was necessary to reconcile disparate measurement extents and spatial scales. Rather than attempting to downscale ECOSTRESS, we up-scaled FLIR to create a thermal image that emulates ECOSTRESS' spatial resolution. To do this, we used FLIR measurements to define temperatures of "pure" ECOSTRESS pixel components: oaks, pines, and sunlit and shaded grass. We converted those temperatures to energies and calculated the FLIR analog for each ECOSTRESS pixel via weighted average, with weights corresponding to the pixel-level prevalence of the pixel components.

$$\text{FLIR} - \text{based temperature}_{70x70m} = \text{Planck}^{-1}\left[\sum_{i=1}^{i=n_{veg}} \text{fraction}_i * \text{energy}_i\right], \quad (1)$$

where "Planck" is Planck's Law, used to convert between temperature and energy, n_{veg} is equal to four (sunlit grass, shaded grass, oak, and pine), "fraction" is fractional cover determined using the vegetation classification, digital surface model, and solar and sensor geometries, and "energy" is aggregated from all ROIs of each vegetation type, as described. Finally, we re-converted energy to temperature.

The temperature of shaded grass was defined as the mean of the lowest quartile of grass pixels, while sunlit grass temperature was the mean of the highest quartile. Definitions of oak and pine temperatures depended on the FLIR map version: for the bulk version, pure oak and pine temperatures were the temperatures associated with the mean energy of all oak or pine pixels in every calibrated oak or pine ROI, respectively. For the "top" version, oak and pine temperatures were mean oak and pine top temperatures, respectively; for the "bottom" version, oak and pine temperatures were mean oak and pine bottom temperatures. In five additional versions, the FLIR map was based on only one of the "pure" components: sunlit grass only, shaded grass only, all grass, bulk oak only, or bulk pine only. FLIR-based temperatures based on single components were invariant across each scene.

We quantified uncertainty intervals associated with the difference between ECOSTRESS and FLIR measurements according to Eqn. 2:

$$\text{ECOSTRESS} - \text{FLIR}_{error} = \sqrt{\text{FLIR}_{error}^2 + \text{ECOSTRESS}_{error}^2}, \quad (2)$$

where FLIR_{error} was based on the difference between the FLIR and reference measurements, as described, and ECOSTRESS_{error} was as reported.

2.4. Data visualization and statistical analyses

To elucidate vertical patterns of intra-canopy (top vs. bottom) and ecosystem component (bulk pine vs. oak vs. grass) temperatures, we plotted diurnal temperature dynamics. We explored environmental correlates of the vertical patterns of intra-canopy temperatures by comparing bottom minus top canopy temperature differences with over- minus under-story shortwave radiation, longwave radiation, air temperature, wind speed, and vapor pressure deficit, as well as with turbulence (ustar) and oak trunk temperature (measured via infrared thermometer).

To assess the correspondence between ECOSTRESS measurements and spatially-explicit FLIR-based temperatures, we compared pixel and mean scene temperature values, and we examined comparative scene temperature variability. To determine the relevance of FLIR end-member choices (canopy tops vs. bottoms vs. bulk; oaks vs. pines vs. sunlit grass vs. shaded grass vs. a hillshade-informed weighted combination of all) to the comparison with ECOSTRESS, we compared distributions of ECOSTRESS - FLIR mean scene temperature differences, with the FLIR values as calculated using the various choices. We assessed statistical significance of these different end-member choices using one-way ANOVAs and post-hoc Tukey HSD tests to compare means, and using Komolgorov-Smirnov tests to compare distributions.

3. Results

3.1. Vertical temperature heterogeneity

3.1.1. Within tree canopies

Hypothesis 1a, that the upper leaves in tree canopies would be warmer than the lower leaves, particularly at times of high incoming solar radiation, was not supported by thermal camera measurements. Rather, the opposite was true: for both oaks and pines during the day, temperatures of the lower canopy were warmer than temperatures of the upper canopy (Fig. 4). This pattern was stronger in oaks compared to pines; however, it was remarkably consistent across all tree ROIs despite variability in ROI shapes and pixel sizes, in canopy height above the ground, and in crown geometries (Fig. S10). At night, the mean temperature of oak canopy tops and bottoms equalized, while mean pine canopy bottoms were typically slightly cooler than tops (Fig. 4).

The daytime difference in temperatures between the tops and bottoms of the canopies was moderately positively correlated with the daytime difference between over- and under-story SW radiation (Spearman correlation $\rho = 0.50$, Fig. 5a) and moderately negatively correlated with the daytime difference between over- and under-story LW radiation, air temperature, and vapor pressure deficit ($\rho = -0.47$, -0.50, and -0.50, Fig. 5b, c, d). Conversely, the daytime canopy temperature differences were not highly correlated with daytime differences between over- and under-story wind speed ($\rho = -0.01$, Fig. 5e); turbulence was more relevant ($\rho = 0.34$, Fig. 5f). Additionally, the daytime canopy temperature vertical difference was correlated with daytime oak trunk temperature ($\rho = 0.35$, Fig. 5g).

Hypothesis 1b, that tree canopies would be more thermally homogeneous at night than during the day, was supported, particularly for oaks: over the full time series of images, the mean daytime (incoming shortwave radiation > 0 W/m^2) temperature difference between oak canopy top and bottom thirds was 0.48°C (standard deviation = 0.72); between pine canopy top and bottom thirds, the mean difference was 0.31°C (sd = 0.49). Considering only times when incoming solar radiation was greater than its mean daytime value (516 W/m^2), the mean difference between oak canopy top and bottom thirds increased to 0.75°C (sd = 0.77), while the mean difference between pine canopy top and bottom thirds was 0.51°C (sd = 0.34). During the night (incoming shortwave radiation = 0 W/m^2), canopy bottoms were slightly cooler than canopy tops (oak: mean difference = −0.05°C, sd = 0.34; pine: mean difference = −0.52 °C, sd = 0.62). At night, canopy temperature differences were less strongly correlated with all micro-climatic gradients except for wind speed (Fig. 5), but they were most highly correlated with the night-time air temperature gradient ($\rho = -0.41$, Fig. 5c). Please see supplemental Fig. S11 for discussion of other, finer-scale diurnal patterns.

3.1.2. Among trees and grass

Oaks, pines, and grass exhibited similar patterns of warming and cooling throughout the day (Fig. 6). During the morning hours before sunrise, all three were slowly cooling at a rate comparable to that of air (0.2–0.3°C per hour). Following sunrise, plant temperatures rose increasingly quickly for 2–4 h and then continued to rise more slowly until early afternoon. In the case of oaks and pines, the usual peak warming rate was centered at 06:00 (bulk oak canopies: 1.9°C/h with a standard error of 0.2°C; pine canopies: 1.5°C/h with a standard error of 0.2°C). Grass warming peaked later in the morning and at a higher value (3.4°C/h, se = 0.3°C at 07:30), while the air changed temperature comparatively slowly, reaching a maximum warming rate of only 1.0°C/h (se = 0.2°C). Grass started cooling first, beginning around 12:30, followed by oaks (at around 14:30) and pines (at around 15:00). The air did not begin to cool until about 16:00. Temperatures then fell increasingly quickly until late afternoon (oak peak cooling: 1.8°C/h at 18:30; pine peak cooling: 1.6°C/h at 18:30; grass peak cooling: 2.5°C/h at 17:30; air peak cooling: 1.2°C/h at 19:00), followed by slower cooling until the next sunrise. During the day, vegetation temperatures nearly always changed more quickly than air temperature, with grass warming and cooling the fastest, then oak, then pine (Fig. 6).

Comparisons of bulk temperatures among the vegetated components of the ecosystem demonstrate that vertical temperature heterogeneity was present not only within canopies, but also across ecosystem

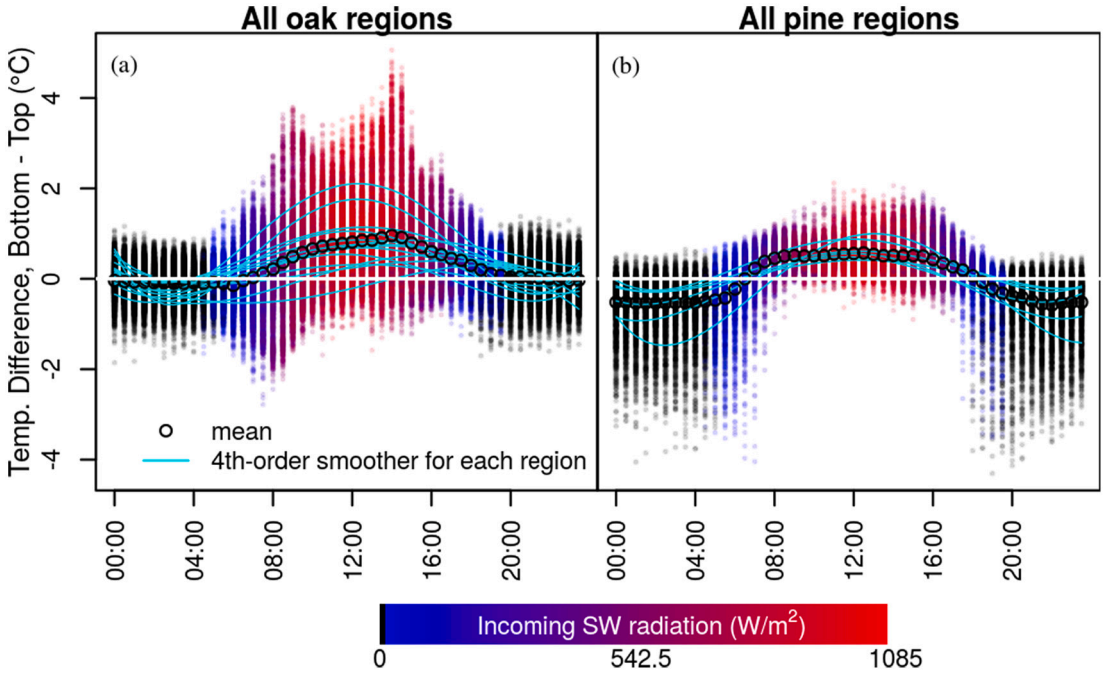

Fig. 4. Oak (a) and pine (b) canopy tops were typically cooler than canopy bottoms during the day, and often slightly cooler during the night. $N = 170{,}744$ points for the *Quercus douglasii* (QUDO) plots (20 oak ROIs x 12,148 images), and $n = 73{,}176$ data points from the *Pinus sabiniana* (PISA) plots (6 pine ROIs x 12,148 images). Points are colored by incoming shortwave radiation, means are denoted by open circles, and cyan lines are fourth-order smoothers, fit to data from each tree ROI individually. (For color, the reader is referred to the web version of this article.)

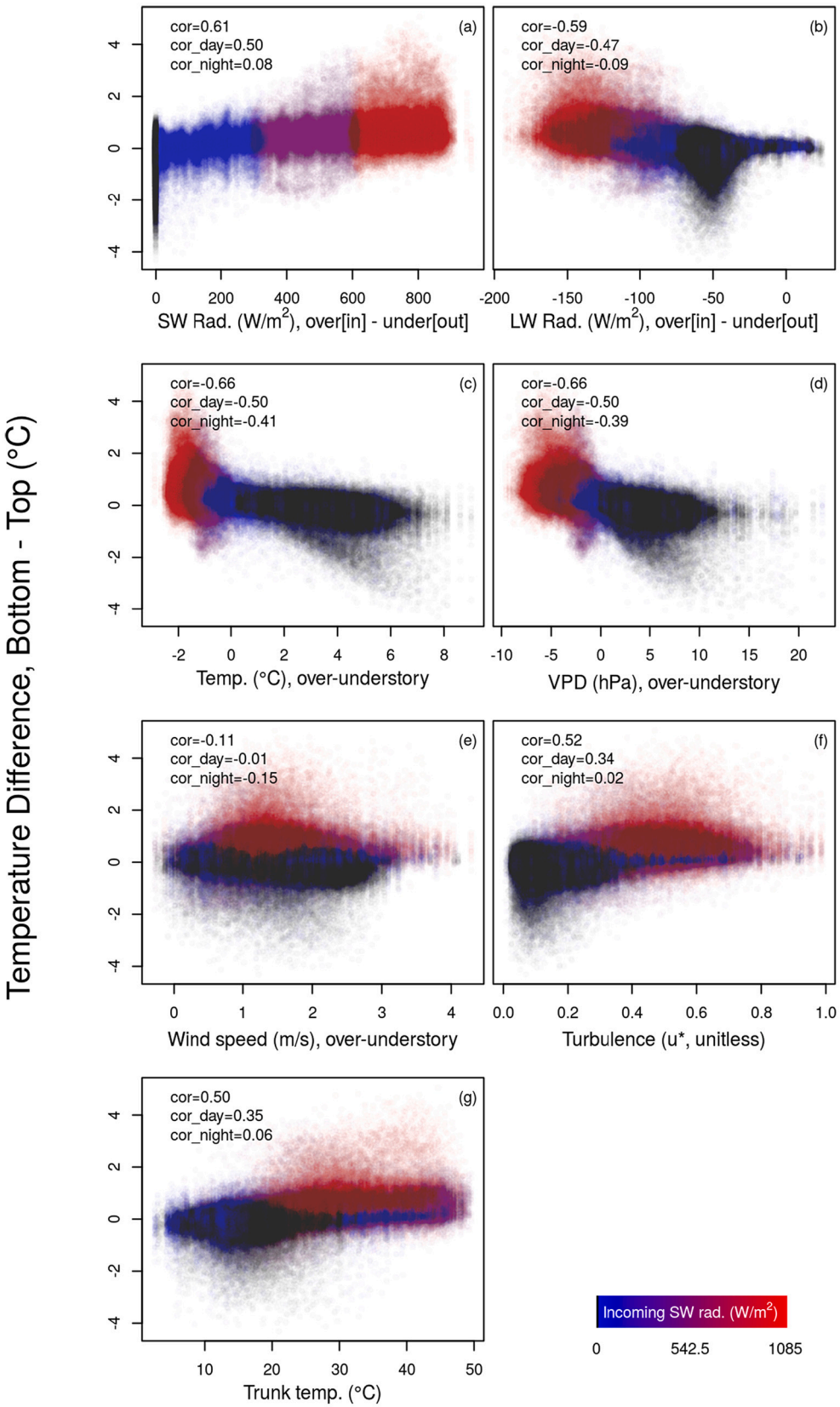

Fig. 5. Relationships between the canopy temperature differences (including both oaks and pines) and (a) incoming SW radiation measured over the canopy minus outgoing SW radiation measured in the under-story; (b) incoming LW radiation measured over the canopy minus outgoing LW radiation measured in the under-story; (c) over- minus under-story air temperature; (d) over- minus under-story VPD; (e) over- minus under-story wind speed; (f) turbulence (reported as "ustar" by Ameriflux); and (g) oak trunk temperature, measured via infrared thermometer. "cor" denotes Spearman correlations. (For color, the reader is referred to the web version of this article.)

vegetation functional types. Hypothesis 1c, that tree leaves would be consistently cooler than the under-story grass, was partially supported: taller vegetation (pines and oaks) was considerably cooler than the senesced grass under-story during the day, but it was typically warmer during the night (Fig. 7a, b). When incoming shortwave radiation was positive, the mean difference between average grass and average oak temperatures was 4.3°C (sd = 5.0); the mean difference between average pine and average grass temperatures was 4.4°C (sd = 5.7).

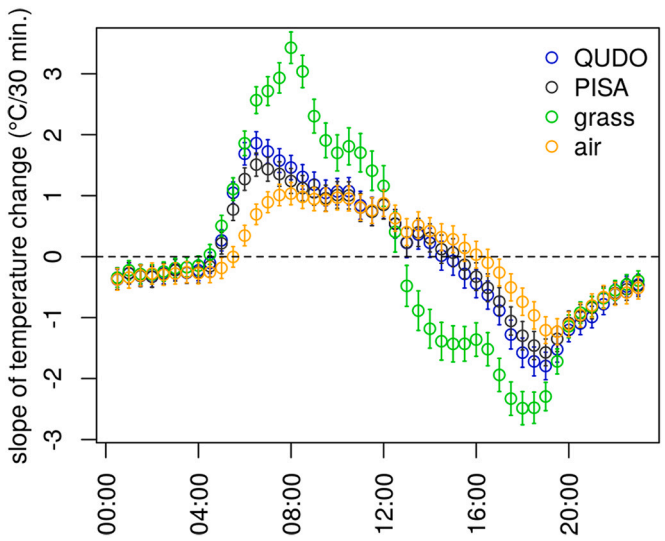

Fig. 6. Slopes of bulk oak, pine, and under-story grass temperature changes throughout the day (including all days in the measurement period), calculated in a moving window of 1.5 h. Error bars are ± 1 standard error of the slope estimate. X-axis labels are the center of the moving window. (For color, the reader is referred to the web version of this article.)

During times of high incoming shortwave radiation (> 516 W/m^2, the mean daytime value), grass temperatures were, on average, 8.0°C warmer than mean oak temperatures (sd = 3.6°C), and 8.7°C warmer than mean pine temperatures (sd = 3.9°C). At night, grasses were an average of 2.0°C cooler than oaks (sd = 1.2°C) and 3.6°C cooler than pines (sd = 1.7°C).

Between the two taller (tree) vegetation types, temperatures were more similar than between either tree type and the grass (Fig. 7c). Oaks were, on average 0.2°C warmer than pines during the day (sd = 0.9°C), 0.7°C warmer during the > 516 W/m^2 part of the day (sd = 0.7°C), and 1.6°C cooler during the night (sd = 0.8°C). Pines nearly always experienced lower diurnal temperature variability than oaks: on average, the daily range of pine temperatures was 2.3°C lower than the range of oak temperatures (sd = 1.0°C).

3.2. Comparison of thermal camera and satellite temperature estimates

Despite the consistent patterns of intra-canopy vertical temperature, Hypothesis 2a – that ECOSTRESS and FLIR temperatures would align more closely when FLIR temperatures were calculated using top-of-canopy measurements rather than bulk average, or bottom-of-canopy measurements – was refuted (Fig. 8, left-most three boxes). There were no statistically significant differences in either means or distributions of ECOSTRESS vs. FLIR comparisons based on FLIR canopy vertical end-member choice (ANOVA means comparison: $F(1,157) = 0, p = 0.99$; Komolgorov-Smirnov pairwise distribution comparisons: D = 0.08, 0.09, 0.11, $p = 1.00, 0.98, 0.89$). Rather, the mix of vegetation included in the FLIR calculations was more relevant, emphasizing the relative importance of plant functional type in extrapolating FLIR measurements, compared to intra-canopy vertical heterogeneity (Fig. 8). In particular, grass cover was important: there was a significant difference between FLIR - ECOSTRESS distribution means when FLIR temperatures were calculated using only sunlit grass temperature vs. all other options ($F(5,287) = 7.01$, $p<0.001$), and there were significant differences between all distributions except: the three weighted options and oak only (D = 0.15, $p = 0.59$), and oak only and all grass (D = 0.21, $p = 0.21$, Fig. 8).

The relative unimportance of intra-canopy thermal gradients in the FLIR/ECOSTRESS comparison is not surprising given the small magnitude of the gradients compared to the divergence between camera and ECOSTRESS temperatures. At the spatial scale of scenes (116–142 pixels), mean ECOSTRESS and FLIR-based surface temperature measurements were strongly related (Fig. 9a, Pearson correlation coefficient = 0.98, $n = 53$). However, during the daytime, they diverged notably, with >60% of daytime scene differences (17 of 28) exceeding the combined ECOSTRESS and FLIR errors (Fig. 9c). While the average daytime difference between mean FLIR scene temperature and mean ECOSTRESS scene temperature was only −0.3°C (sd = 3.4°C), the mean of absolute daytime temperature differences was 2.6°C (sd = 2.1°C), as ECOSTRESS temperatures were typically warmer during high light and FLIR temperatures were warmer during low light (Fig. 9a, c). Conversely, all but four (of 25) night-time differences between ECOSTRESS and FLIR-based mean scene temperatures were within combined ECOSTRESS and camera margins of error, with FLIR temperatures generally a fractional degree warmer (mean absolute difference between FLIR and ECOSTRESS was 0.8°C [sd = 0.5°C]). Within scenes, though the ECOSTRESS - FLIR pixel-scale mismatches were often somewhat autocorrelated, high mismatches were not consistently attributable to any particular part of the study area (Fig. 10).

These results are not substantively different given different definitions of shaded and sunlit grass end-members. For example, when sunlit and shaded grass are both assigned mean grass temperature, the average

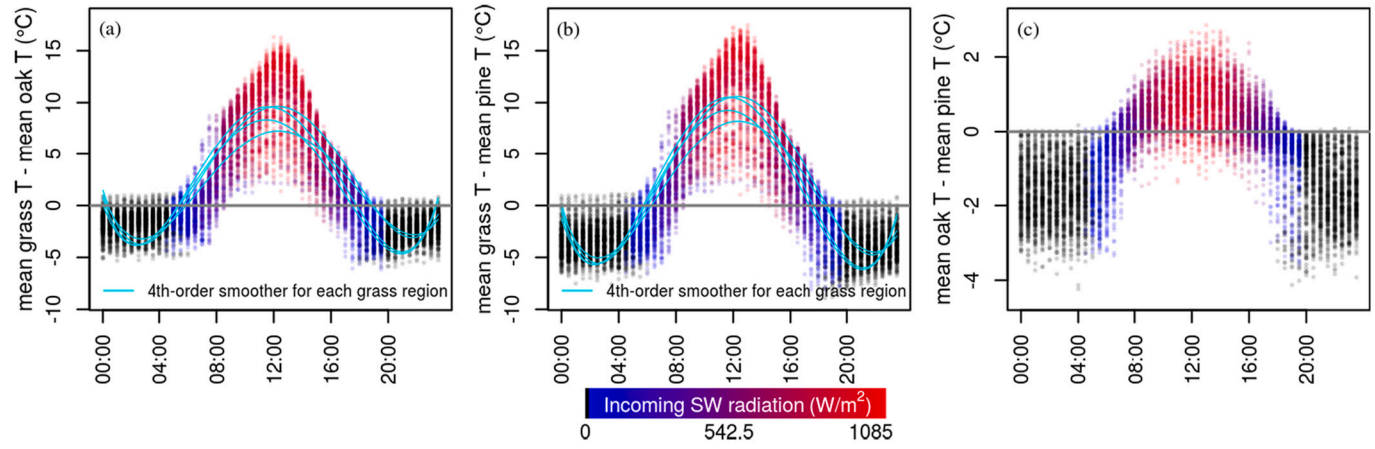

Fig. 7. Comparisons between mean grass temperatures and (a) mean oak temperatures and (b) mean pine temperatures. Points ($n = 12{,}148$) are means across ROIs, and the cyan lines show the smoothed relationships between mean tree temperatures and the grass ROIs separately. Panel (c) shows a comparison between mean oak and mean pine temperatures. Colors are linearly scaled according to incoming shortwave radiation. Note that (a) and (b) share a y-axis, while (c) is scaled differently. (For color, the reader is referred to the web version of this article.)

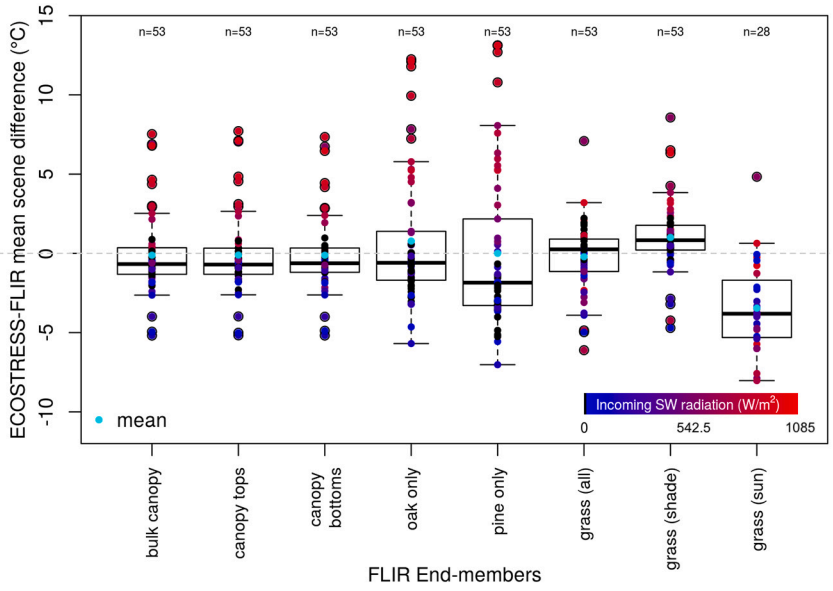

Fig. 8. Distributions of FLIR-ECOSTRESS mean scene temperatures when FLIR temperatures were calculated in different ways. From left to right: FLIR temperatures calculated based on weighted abundances of vegetation types in a pixel using bulk canopy temperatures as tree end-members; FLIR temperatures calculated based on weighted abundances of vegetation types in a pixel using canopy top temperatures as tree end-members; FLIR temperatures calculated based on weighted abundances of vegetation types in a pixel using canopy bottom temperatures as tree end-members; FLIR temperatures calculated as though the entire pixel were (bulk) oak, as though the entire pixel were (bulk) pine; as though the entire pixel were (bulk) grass; as though the entire pixel were shaded grass; and as though the entire pixel were sunlit grass. Please see text for statistical significance. (For color, the reader is referred to the web version of this article.)

daytime difference between mean FLIR scene temperature and mean ECOSTRESS scene temperature is −1.1°C (sd = 3.6°C), and the average absolute difference is 2.8°C (sd = 2.5°C). When shaded grass is the mean of grass pixel temperatures and sunlit grass is the mean of the top 5% of grass pixel temperatures (an extreme choice intended to push the FLIR measurements closer to ECOSTRESS measurements), the average daytime difference between mean FLIR scene temperature and mean ECOSTRESS scene temperature is 0.1°C (sd = 3.3°C), but the average absolute difference is 2.7°C (sd = 1.9°C).

Hypothesis 2b, that ECOSTRESS and FLIR thermal measurements would deviate most at times of highest thermal heterogeneity and least at times of lowest thermal heterogeneity, was partially supported, in that the largest absolute differences between FLIR and ECOSTRESS tended to be at times of high horizontal thermal heterogeneity (Fig. 9a, Pearson correlation between absolute ECOSTRESS - FLIR mean scene difference and FLIR [ECOSTRESS] IQR = 0.38 [0.56]). However, attribution of temperature heterogeneity as the cause of the high mismatches between ECOSTRESS and FLIR temperature estimates was not straightforward because thermal heterogeneity was strongly associated with higher incoming SW radiation (Fig. 9b; correlation between incoming SW and the inter-quartile range of the ECOSTRESS [FLIR] scene temperatures was $r = 0.91$ [0.84]). Results of regression models indicate that SW radiation is the stronger predictor of the mismatches: considering only one of the correlated predictors as a candidate (ECOSTRESS IQR, FLIR IQR, or incoming SW), we found that the model including SW radiation was most explanatory (Adjusted $R^2 = 0.71$ vs. 0.49 and 0.36 for models substituting ECOSTRESS scene IQR and FLIR scene IQR predictors for SW predictors, respectively), and it showed less residual pattern (models not shown). It is likely, therefore, that SW radiation underlies both the thermal heterogeneity and the FLIR/ECOSTRESS mismatch.

There was a clear quadratic relationship between the mean ECOSTRESS - FLIR scene temperatures and daytime incoming SW radiation (Fig. 9c). At low levels of incoming SW, ECOSTRESS measurements were cooler than FLIR measurements: in the lowest quartile of incoming SW ($0 < SW < 223 W/m^2$), the average ECOSTRESS - FLIR mean scene temperature difference was −2.4C (range = −5.2 to −0.5C, $n = 7$ scenes). As incoming SW radiation increased, ECOSTRESS temperatures became increasingly warmer than FLIR temperatures: in the highest quartile of incoming SW ($> 765 W/m^2$), the average ECOSTRESS - FLIR mean scene temperature difference was 4.2°C (range = 0.4 to 7.5°C, n = 7 scenes).

Land surface temperature errors reported by ECOSTRESS were not associated with incoming SW radiation (mean daytime scene error = 1.4°C, sd = 0.3°C, range 0.9–1.9°C; mean night-time scene error = 1.4°C, sd = 0.3°C, range = 0.9–2.2°C; Pearson correlation between SW and error = −0.07, Fig. S12). FLIR errors tended to have a larger range: positive error ranged from 0 to 3.7°C (mean = 0.5°C, sd = 1.1°C), and negative error ranged from 0 to 3.5°C (mean = 1.7 °C, sd = 0.7°C). FLIR positive error was strongly associated with incoming SW (Pearson correlation = 0.76, Fig. S12), and rose sharply after about 600 W/m^2 of incoming SW radiation.

Within-scene ECOSTRESS and FLIR pixel correlations were considerably weaker than the across-scene mean temperature correlation. The mean Pearson correlation between ECOSTRESS and FLIR-based pixel temperatures within daytime scenes was 0.50 (sd = 0.36), and the mean night-time pixel correlation was 0.097, (sd = 0.34; Fig. S13). The inter-quartile ranges of pixel values in ECOSTRESS vs. FLIR-based scenes were strongly related (Pearson correlation = 0.88, Fig. 9b), with darker scenes having lower thermal variability in both cases. FLIR scenes were nearly always more thermally variable than ECOSTRESS scenes at times of higher SW radiation, but the difference in pixel variability (Fig. 9b) was small compared to the absolute temperature differences (Fig. 9a): maximum difference in IQR was 1.8°C; mean daytime absolute IQR difference was 0.5°C (sd = 0.5°C). Please see supplemental section S14 for additional analysis and discussion of the relationships between ECOSTRESS and FLIR thermal measurements and environmental conditions.

4. Discussion

4.1. Intra-canopy temperature gradients

We found that the lower parts of tree canopies were consistently warmer than canopy tops during the day. This pattern is the opposite of the pattern reported by the few other studies measuring the vertical distribution of leaf temperatures within canopies: Martin et al. (1999) found that needles on upper branches of *Abies amabilis* reached higher temperatures than leaves on lower branches in the sub-alpine zone of the Cascade mountains; Fauset et al. (2018) suggested that leaves positioned higher in the canopy of a Brazilian Atlantic forest were more commonly warmer than air temperature than lower leaves; Rey-Sánchez et al. (2016) used structural equation modeling to show that leaf temperature in a semi-deciduous Panamanian tropical forest was largely controlled

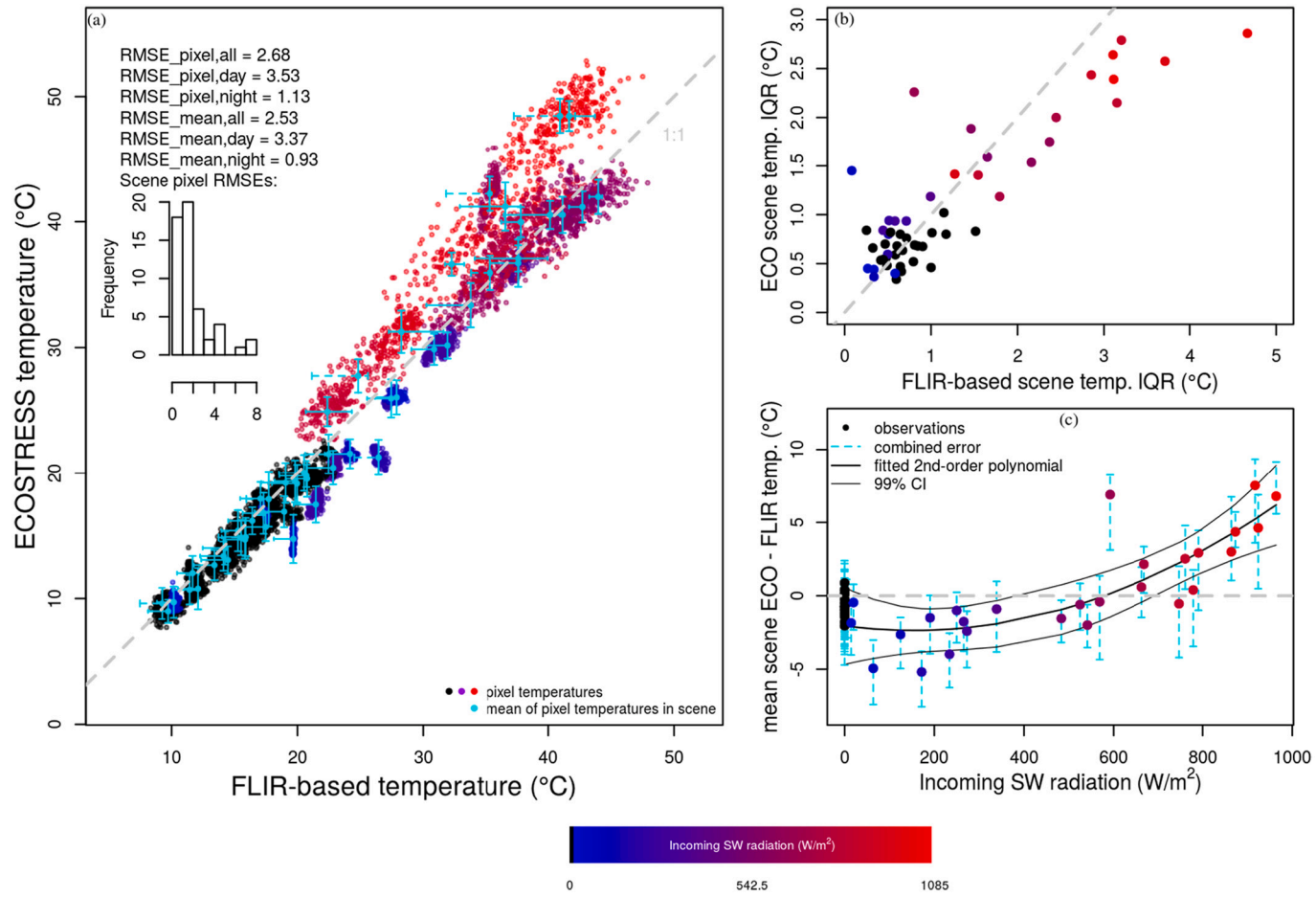

Fig. 9. (a) Comparison of ECOSTRESS and FLIR-based temperatures, where FLIR-based temperatures were calculated according to Eqn. 1. Points colored by incoming shortwave radiation are individual pixels ($n = 6635$ pixels in 53 total scenes). Cyan points are the average temperature value for each scene ($n = 53$). Error bars in the ± y direction are the mean of pixel-wise ECOSTRESS-reported errors for each scene. Error bars in the x direction are the differences between mean FLIR measurement of the concrete reference panel and the IRT and/or mean thermocouple measurement of the panel. When the bar is only in the negative direction, both the IRT and the mean TC measurements were cooler than the FLIR. When the bar is only in the positive direction, both the IRT and the mean TC measurements were warmer than the FLIR. In either case, the length of the bar is the larger of the offests. Bars in both x directions denote that one of the reference measurements was higher that the FLIR, one lower. When FLIR errors were estimated, x error bars are dashed. (b) Comparison of ECOSTRESS and FLIR-based scene interquartile temperature ranges (75th - 25th quartiles). (c) Relationship between incoming SW radiation and the mean scene ECOSTRESS - FLIR mismatch. The polynomial is fitted only to daytime data (SW > 0 W/m^2), and the error bars show the error associated with the difference between ECOSTRESS and FLIR (Eqn. 2), calculated separately in the positive and negative directions. (For color, the reader is referred to the web version of this article.)

by incident photosynthetic photon flux density in the wet season and by air temperature in the dry season. They found that, given the gradients of these drivers, upper-canopy leaves were warmer than shade leaves. Most recently, Miller et al. (2021) reported that the temperature of the upper (sunlit) foliage in the Puerto Rican wet tropics exceeded the temperature of lower (shaded) foliage by up to 4°C.

We propose that the inverse thermal gradient observed in this study results from the sparse nature of woodland savanna trees and tree canopies. In closed-canopy ecosystems, solar illumination is a dominant control of relative leaf temperature (Doughty and Goulden, 2008; Rey-Sánchez et al., 2016). Because sunlight comes from above, leaves positioned higher in the canopy are comparatively warmer (note that microclimate, physiology, and canopy/leaf structure/shape also play a role [Blonder and Michaletz, 2018; Smith and Nobel, 1977; Woods et al., 2018]). In contrast, in sparser woodland savanna tree canopies, such as at our US-Ton study site, the thermal gradient becomes inverted because: (i) solar radiation undergoes less attenuation by tree canopies, (ii) lateral light interception by most trees is unhindered by neighbors, and (iii) there are large areas in which solar radiation is directly incident on the grassy under-story. Indeed, at our study site, measurements of incoming and outgoing SW radiation at 21.5 m vs. 1.06 m above ground level are remarkably similar (Fig. S15a).

These differences in canopy structure have important implications for both the radiative and the temperature components of woodland savanna micro-environments. First, because the grass gets very warm (Fig. 7), significant longwave (LW) radiation is incident on the tree canopies from below (Fig. S15b). Assuming that attenuation of upwelling LW radiation by the air between grass and canopy is negligible, we expect that the magnitude of incident LW radiation from below is, on average, about 70% of the magnitude of incident SW radiation at the time when the canopy temperature gradient is most pronounced (14:00). This is a considerable radiative flux. Second, because SW radiation is often directly incident on the grass, some portion is reflected onto the bottom of the tree canopy due to the grass albedo (on average, about 15% of incoming SW at 14:00). Incident radiation from either direction will permeate through the canopy approximately according to Beer's Law (Campbell and Norman, 1998). Because the tree leaf area index in this ecosystem is relatively low (typically <1) and summertime solar elevation is high, it is reasonable to assume 60–80% transmittance (Monson and Baldocchi, 2014); this would yield approximately balanced radiative loading on the canopy tops and bottoms – in marked contrast to the strongly asymmetric radiative loading in closed-canopy

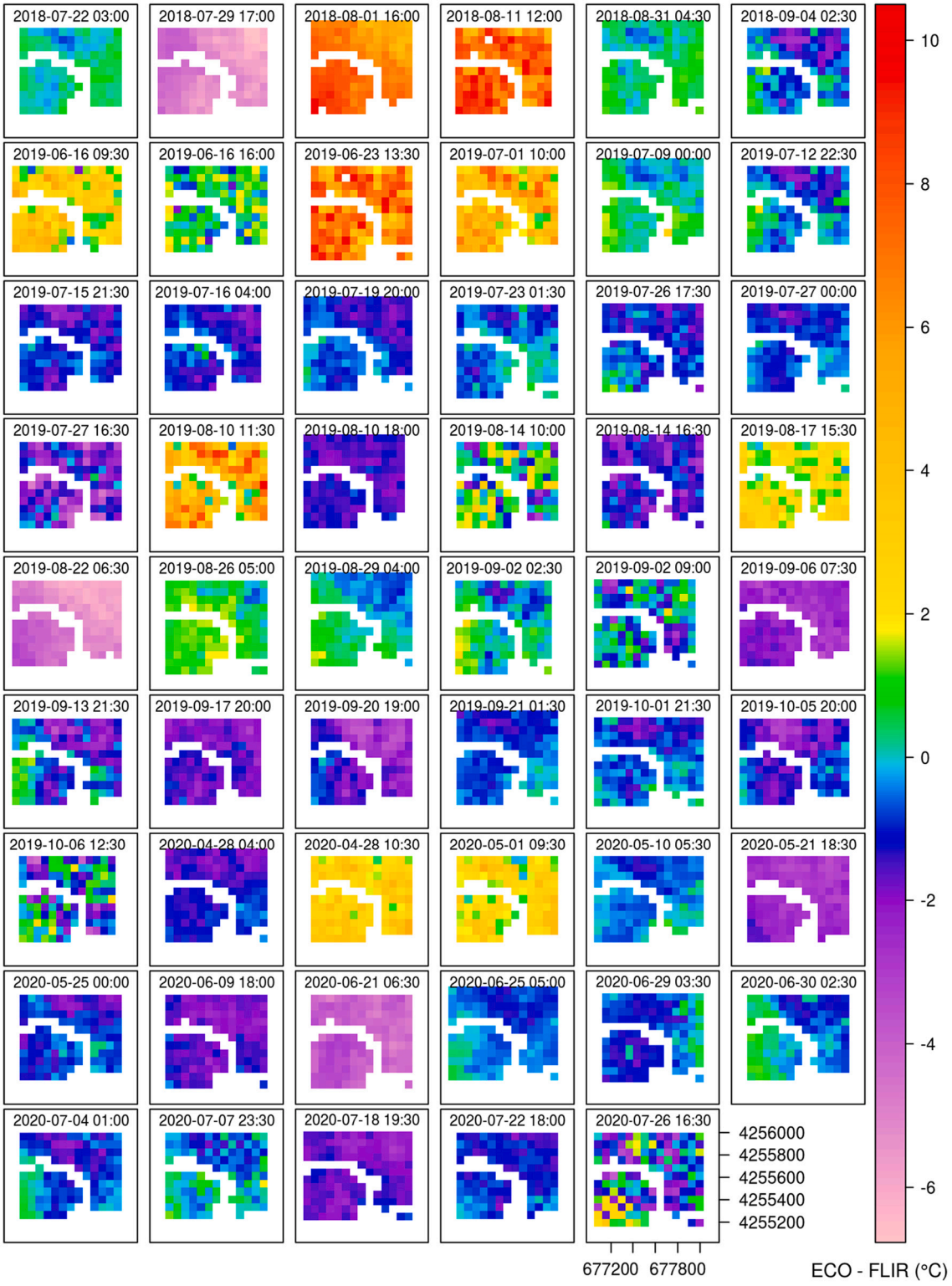

Fig. 10. ECOSTRESS - FLIR difference images for the 53 ECOSTRESS acquisitions corresponding to FLIR collection times. Masked areas are pixels intersecting the road, pond, and infrastructure. Map units are UTM 10 N, and date-time labels are FLIR collection times in PST. (For color, the reader is referred to the web version of this article.)

forests.

An approximately balanced radiation load would not, by itself, produce the observed inverse temperature gradients: microclimate and canopy turbulent energy fluxes likely also play a role. Unlike in forested ecosystems (e.g. Renaud et al., 2011; Davis et al., 2019), midday air temperature and vapor pressure deficit are typically higher in the woodland savanna under-story than the over-story (Fig. 5c and d; likely associated with the sensible heat flux emanating from the hot grass). Higher air temperature would make it comparatively less favorable for lower leaves to convect sensible heat, and higher vapor pressure deficit (at relatively consistent and low soil moisture in the dry season) would tend to decrease stomatal apertures and depress latent energy flux of

lower leaves (Lange et al., 1971), both of which would cause relative warming.

The canopy temperature gradients were also correlated with turbulence: increasing turbulence was correlated with comparatively warmer canopy bottoms (Fig. 5f). Stronger coupling of the upper canopy leaves to the atmosphere might decrease turbulent flux resistance (Jarvis and McNaughton, 1986), increasing the efficiency by which the top of the canopy convects sensible heat. This "convector effect" has been observed by Rotenberg and Yakir (2011) in a semiarid open-canopy pine forest. The higher sensible heat flux observed at the aerodynamically rougher US-Ton site compared to the aerodynamically smoother neighboring US-Var grassland site (Fig. S15c) is suggestive of a similar mechanism here; however, additional research is required to determine whether a convector effect implied from surface energy balance analyses can occur the scale of individual tree crowns. Finally, it is notable that the temperature of bark (and likely also the branches) exceeds leaf temperatures in the early afternoon by several degrees, and that bark temperature is positively correlated with canopy-bottom minus canopy-top temperature (Fig. 5g). Kobayashi et al. (2012) estimated that 12% of available energy at US-Ton is stored in the woody elements. If the lower canopy is subject to larger or more numerous woody elements, this may also have a significant warming influence.

Temporal variations in thermal patterns support these proposed mechanisms. At night, vertical temperature differences are smaller, and the canopy tops tend to be slightly warmer (Fig. 4). While night-time radiative fluxes are similar at different vertical heights (Fig. S15), lower mean air temperature and vapor pressure deficit in the understory would favor this pattern (Fig. 5c, d). In the early mornings, some oak tops are briefly warmer than oak bottoms (Fig. S10). This likely arises because of the rapid warming of the canopy tops in the early morning (Fig. S11a) due to SW radiation increasing, but before the grass has warmed (Fig. 7), while over-story and under-story air temperature and vapor pressure deficit are comparable (Fig. 5c, d), and woody elements are still cool. More research is required to understand why some canopies exhibit more temporally auto-correlated patterns of warming morning - midday (Fig. S11d) while others are more temporally auto-correlated in the afternoon (Fig. S11c), but we expect that this is related to landscape position with respect to sunlight, neighbors, and shading patterns.

Overall, we suggest that the daytime pattern of warmer bottoms and cooler tops of woodland savanna trees is the result of a suite of co-acting mechanisms: radiative warming of the lower canopy by the grass (both LW and SW), microclimatic gradients comparatively unfavorable to sensible and latent flux from the lower canopy, and warm woody elements (likely) lower in the canopy. Based on energy magnitudes and the overall positive correlation between the SW gradient and the canopy temperature gradient (Fig. 5a), we conjecture that LW radiative warming of the lower canopy by the grass is the dominant player; however, disentangling the effects of each driver on the thermal gradient would benefit from further research. In particular, (i) deployment of additional radiometers directly under canopies of interest would help resolve the within-canopy radiation environment; (ii) a higher-resolution thermal camera would minimize possible contamination of leaf measurements by (likely) warmer branches, and (iii) comparison of vertical thermal gradients present in individuals existing in denser vs. more open areas would help elucidate the relevance of the convector effect (Rotenberg and Yakir, 2011). Three-dimensional modeling studies (e.g. using CANOAK-FLiES [Kobayashi et al., 2012] or the Radiation Absorption, Transpiration, and Photosynthesis model [Sinoquet et al., 2001; Woods et al., 2018]) could also help clarify the factors responsible for the observed thermal gradients.

The fact that the intra-canopy temperature gradients we report are inherently temperature differences (rather than absolute temperatures) makes them relatively robust to FLIR sensor and thermal image calibration error. However, given their relatively low magnitudes (Fig. 4) compared to plausible camera error (Fig. S8), it is useful to address the most likely confounding influence on these relative measurements explicitly: the source of reflected radiation. Radiation from any target's surroundings reflects off that target and contributes to its apparent temperature. Correcting target temperatures for reflected radiation involves subtracting a reflection term from the sensor reading (Aubrecht et al., 2016; Johnston et al., 2021). Therefore, if the reflected energy originates from a cold source (e.g. the sky), the corrected target temperature will be relatively higher than if the reflected energy originates from a warm source (e.g. the ground). In calibrating tree canopy temperatures, we assumed that radiation reflected by all canopy vertical layers originated from the sky. Our results are essentially the same as they would be given any formulation in which radiation reflected by the canopy layers is the same, regardless of the magnitude of that reflection. However, gradients could be somewhat changed if reflected radiation were different for different sections of the canopy. Given the direction of the daytime canopy temperature gradients we report, the most conservative formulation would be for 100% of the radiation reflecting off canopy tops to be from the sky (making calibrated top temperatures as warm as possible), and 100% of radiation reflecting off canopy bottoms to be from the ground (making calibrated bottom temperatures as cool as possible). This is, in reality, very unrealistic: each canopy layer would actually reflect radiation from some combination of sky, other canopy leaves/branches, and the grass/ground. Regardless, results based on this overly-conservative formulation demonstrate that our findings regarding the diurnal thermal gradients in tree canopies are robust: daytime canopy tops are (often) cooler than canopy bottoms for 11/14 oak ROIs and 5/6 pine ROIs (Fig. S16).

Importantly, when temperature differences are larger than the intra-canopy gradients (as they are between ecosystem vegetation components or between FLIR and ECOSTRESS), the relevance of reflected radiation source in this ecosystem is relatively low, due to the high emissivities of ecosystem components (Johnston et al., 2021).

4.2. Temperature variability among plant types

While the intra-canopy pattern of vertical temperature gradients were surprising, thermal relationships among plant components in the ecosystem were as we expected: pine canopy temperatures followed air temperature more closely than oak canopy temperatures and understory grasses experienced both faster warming to higher peak temperatures and faster cooling (Fig. 6). Regarding the difference between pines and oaks, it has long been understood that smaller leaves such as pine needles have higher boundary layer conductances and are therefore more strongly coupled to the atmosphere (e.g. Gates et al., 1968). Additionally, in this ecosystem, mature pines are taller than their oak neighbors, which would tend to further reduce the comparative leaf aerodynamic resistance of the pine foliage (Wilson et al., 1987). Regarding the faster warming and cooling of the grasses and their higher daytime peak temperatures, three important factors likely contribute to this effect: (i) due to its very low water content, particularly during the dry season, the grass foliage has a lower thermal inertia (lower heat capacity) and thus will tend to change temperature faster than the trees (McAllister et al., 2012); (ii) the senescent state of the grass canopy during the time of study means that there is a consequent lack of latent cooling; (iii) relative aerodynamic smoothness of the grass reduces heat loss via turbulent transfer of sensible heat (Rotenberg and Yakir, 2011); and (iv) the grass is most proximal to soil which, when sunlit, may exceed 50 — and occasionally 60 — °C in the summertime (Johnston et al., 2021).

4.3. ECOSTRESS and thermal camera temperature comparison

In this research, we employed methods designed to reconcile the geographic and view angle incompatibilities between a satellite thermal sensor and a tower-mounted thermal camera, pointed laterally at a Mediterranean woodland savanna canopy from 76° off-nadir. Given the

proliferation of each of these data types (e.g. Aubrecht et al., 2016; Pau et al., 2018; Kim et al., 2018; Still et al., 2019; Johnston et al., 2021), the fundamental role played by vegetation temperature in the functioning of plants (Farquhar et al., 1980; Farquhar and Sharkey, 1982; Atkin and Tjoelker, 2003; Michaletz, 2018; Raschke, 1960) and ecosystems (Charney et al., 1975; Shukla and Mintz, 1982), and the omnipresent interest in scaling biological processes from leaves to canopies to landscapes, understanding their correspondence is a priority.

Our scaling methods allowed us to extrapolate the comparatively spatially-isolated camera measurements to the scale of the approximate footprint of the flux tower, yielding high correlations between ECOSTRESS scene temperatures and FLIR-based scene temperatures, as well as between ECOSTRESS scene IQRs and FLIR-based scene IQRs (Fig. 9a, b). Additionally, we found that FLIR and ECOSTRESS thermal measurements were, broadly, responsive to similar environmental drivers (Supplemental section S14). However, the mismatch between ECOSTRESS and FLIR thermal measurements was too large to detect an influence of the physiologically-interesting vertical thermal gradients in the comparisons.

We expected that the FLIR and ECOSTRESS measurements would be in stronger agreement when FLIR tree canopy temperatures were defined as top-of-canopy temperature, rather than bottom-of-canopy or bulk temperature. However, the distributions of FLIR - ECOSTRESS temperatures, given different end-members based on canopy height, were statistically indistinguishable (Fig. 8) – the magnitudes of intra-canopy temperature differences (usually fractional degrees) were very small compared to the differences between FLIR and ECOSTRESS: mean scene temperature differences ranged from −7.5°C to 5.2°C, with a daytime absolute difference mean of 2.6°C and a night-time absolute difference mean of 0.8°C (Fig. 9).

While there were some significant differences in the distributions of the FLIR/ECOSTRESS mean scene mismatch when the FLIR map was more dramatic – e.g. when only a single end-members was defined, such that the entire map was one temperature – the clearest driver of ECOSTRESS/FLIR mismatch was incoming SW radiation. Mismatches were small at night, but FLIR was significantly warmer than ECOSTRESS at low (but > 0) incoming SW radiation, and significantly cooler at high incoming SW radiation (Fig. 9).

Given the significant number of steps required to create a thermal camera-based temperature image for comparison with ECOSTRESS measurements, there are a number of possible contributors to the ECOSTRESS/FLIR mismatch. First is the assumption of FLIR end-member representativeness. We calculated FLIR end-members as the mean temperature of oak and pine regions of interest (ROIs) or, in the case of grass, as the mean of the warmest and coolest quarter of grass ROIs (due its bimodal daytime temperature distribution caused by areas of sun and shade). We then used those end-members to predict temperature across the entire scene according to Eqn. 1. It is a simplification to assume that all oaks, all pines, all shaded grass, and all sunlit grass have the same temperature. Choosing mean values would tend to contract predicted pixel temperature variability, and the invariant nature of the end-members surely contributed to the unexpectedly strong relationship between FLIR-based pixel temperature and canopy cover (Fig. S14).

Second, the area visible to the camera did not encompass the entire range of canopy cover present in a scene (Fig. S6). Overall, however, these two contributors to the mismatch seem to have had only minor consequences, as FLIR-based scene temperature variability was actually greater than ECOSTRESS scene temperature variability (Fig. 9b), and omitting extrapolated pixels from the analyses did not substantively change the results. Alternative selection of sun and shade grass end-member values (both set to the mean value, or shade defined as the mean and sun defined as the mean of the top 5% of values) also did not substantively change the results.

Third, the DSM makes the surface “opaque,” whereas in reality canopies are sparse. The DSM is therefore likely to project more shadows than truly exist, making the FLIR calculations too cool. However, given that the largest mismatches between FLIR and ECOSTRESS were at times of low solar zenith angle, this is also unlikely to have been a large contributor. Fourth, it is likely that the ECOSTRESS sensor images some amount of grass through the sparse canopies, and some amount of soil through the dry grass cover. We did not consider that LAI is often <1 in our weighted average of covers; this would tend to make ECOSTRESS measurements warmer than FLIR-based measurements, particularly during times of high light (as we observed). Finally, FLIR sensor error and image calibration error are other potential sources of error in the thermal-camera-based map: FLIR measurements of the concrete reference panel diverged from independent reference measurements by a mean of 0.9°C (mean of four thermocouples) and 1.1°C (infrared thermometer, Fig. S8). However, even considering the largest likely uncertainty intervals for both the FLIR and ECOSTRESS, there were still significant disagreements between them at times of low and high incoming SW radiation (Fig. 9c).

Caution is also merited in analyses of pixel-scale ECOSTRESS vs. FLIR surface temperatures (Figs. 9a, S14), because ECOSTRESS’ geolocation challenges preclude precise knowledge of measurement locations – errors of about 50 m are typical. It remains valuable, however, to quantify the combined influence of the measurement and geolocation challenges on differences between ground-based and satellite measurements. Further, we expect that comparisons of pixel temperature variability across a scene are robust to sub-pixel-scale geolocation uncertainty, and possible geolocation uncertainty does not have a statistically-significant effect on scene mean temperature comparisons (Fig. S17).

Our comparisons between ECOSTRESS and an independent measurement (FLIR thermal camera) are comparable to those found by Silvestri et al. (2020), who reported pixel-based RMSEs of 0.9–4.2°C for seven instances of approximately concurrent acquisitions of ECOSTRESS, ASTER, and Landsat 8 TIRS over active Italian volcanoes. They are larger than those found by Hook et al. (2020), who report average ECOSTRESS agreement with ground-based measurements of Lake Tahoe and the Salton Sea of 0.7–1.1°C during the day and 1.2–1.6°C at night, depending on the channel. Hook et al.’s tests were more ideal, in that measurements were matched within five minutes and both targets were large and homogeneous, allowing comparisons of radiometer measurements with the average of multiple ECOSTRESS pixels. They also effectively removed uncertainty associated with radiative transfer and the temperature and emissivity separation algorithm (Gillespie et al., 1998) from their analysis by propagating ground measurements to at-sensor radiance and comparing brightness temperatures, rather than surface temperatures.

5. Conclusions

We measured clear and consistent intra-canopy vertical thermal gradients in the woodland savanna study area during the dry season: canopy tops were cooler than canopy bottoms during the day, largely associated with radiative warming from below by the senescent grass under-story. There were also consistent thermal differences between the pine, oak, and grass: grass was considerably warmer than either pine or oak during the day (on average, 4.3°C warmer than oaks and 4.4°C warmer than pines), and slightly cooler at night (on average, 2.0°C cooler than oaks and 3.6°C cooler than pines); pine temperature was more closely coupled to air temperature than oak temperature, and pines tended to be warmer at night and cooler during the day, compared to oaks. In reconciling ECOSTRESS with FLIR in-situ thermal camera measurements, it was important to consider temperature differences between vegetation types, but the magnitude of intra-canopy thermal gradients was negligible compared to the overall magnitude of FLIR/ECOSTRESS mismatch. ECOSTRESS and the in-situ thermal camera measurements were responsive to similar environmental drivers and were in high agreement at night; however, their measurements diverged

at times of low and high incoming SW radiation: ECOSTRESS was cooler just after sunrise, and warmer at times of high incoming SW radiation. Continuing to develop our understanding of the correspondence between ground-measured vegetation temperature and thermal remote sensing will help broaden the applicability of remote sensing data in ecological studies of temperature-mediated community dynamics, as benchmark measurements for terrestrial biosphere model predictions, and as drivers of plant physiological models of temperature-dependent processes. Fruitful future research directions include: mechanistic modeling of within-canopy thermal heterogeneity in savanna ecosystems, use of thermal cameras mounted on un-crewed aerial vehicles (UAVs) to collect more spatially-extensive temperatures with which to compare ECOSTRESS, and examination of the generality of the effect of SW radiation on temperature measurement accuracy in structurally-complex plant canopies.

CRediT authorship contribution statement

Miriam R. Johnston: Conceptualization, Data curation, Formal analysis, Visualization, Writing – original draft, Funding acquisition. **Ana Andreu:** Data curation, Writing – review & editing. **Joseph Verfaillie:** Data curation. **Dennis Baldocchi:** Writing – review & editing, Resources, Funding acquisition. **Paul R. Moorcroft:** Conceptualization, Writing – review & editing, Supervision, Resources, Funding acquisition.

Declaration of Competing Interest

The authors declare that they have no known competing ffnancial interests or personal relationships that could have appeared to infiuence the work reported in this paper.

Acknowledgements

This work was supported by NASA Earth and Space Science Fellowship award NNX16AO21H to M. R. J. and P. R. M., the Harvard University Department of Organismic and Evolutionary Biology, the European Union's Horizon 2020 Research and Innovation program, Marie Sklodowska-Curie grant 703978 to A. A., and NASA award 80NSSC20K0166 to D. B. and J. V. Funding for AmeriFlux core site data was provided by the U.S. Department of Energy's Office of Science. The authors would like to thank Dr. Peter Boucher for lidar consultation and Dr. Elsa Ordway, Dr. Andrew Maguire, and Ms. Nidhi Vinod for useful conversation.

Appendix A. Supplementary data

Supplementary data to this article can be found online at https://doi.org/10.1016/j.rse.2022.112950.

References

Anderson, M.C., Kustas, W.P., Norman, J.M., Hain, C.R., Mecikalski, J.R., Schultz, L., González-Dugo, M.P., Cammalleri, C., D'Urso, G., Pimstein, A., Gao, F., 2011. Mapping daily evapotranspiration at field to continental scales using geostationary and polar orbiting satellite imagery. Hydrol. Earth Syst. Sci. 15, 223–239. https://doi.org/10.5194/hess-15-223-2011.

Atkin, O.K., Tjoelker, M.G., 2003. Thermal acclimation and the dynamic response of plant respiration to temperature. Trends Plant Sci. 8, 343–351. https://doi.org/10.1016/S1360-1385(03)00136-5.

Aubrecht, D., Helliker, B., Goulden, M.L., Roberts, D.A., Still, C.J., Richardson, A.D., 2016. Continuous, long-term, high-frequency thermal imaging of vegetation: uncertainties and recommended best practices. Agric. For. Meteorol. 228-229, 315–326. https://doi.org/10.1016/j.agrformet.2016.07.017.

Baldocchi, D., Ma, S., Verfaillie, J., 2020. On the inter- and intra-annual variability of ecosystem evapotranspiration and water use efficiency of an oak savanna and annual grassland subjected to booms and busts in rainfall. Glob. Chang. Biol. 359–375. https://doi.org/10.1111/gcb.15414.

Banerjee, T., Linn, R., 2018. Effect of vertical canopy architecture on transpiration, thermoregulation and carbon assimilation. Forests 9. https://doi.org/10.3390/f9040198.

Berry, J., Bjorkman, O., 1980. Photosynthetic response and adaptation to temperature in higher plants. Annu. Rev. Plant Physiol. 31, 491–543. https://doi.org/10.1146/annurev.pp.31.060180.002423.

Blonder, B., Michaletz, S.T., 2018. A model for leaf temperature decoupling from air temperature. Agric. For. Meteorol. 262, 354–360. https://doi.org/10.1016/j.agrformet.2018.07.012.

Brown, H.T., Escombe, F., 1905. Researches on some of the physiological processes of green leaves, with special reference to the interchange of energy between the leaf and its surroundings. Proc. R. Soc. B 76, 29–111. https://doi.org/10.1098/rspb.1905.0002.

Brutsaert, W., 1975. On a derivable formula for long-wave radiation from clear skies. Water Resour. Res. 11, 742–744. https://doi.org/10.1029/WR011i005p00742.

Campbell, G.S., Norman, J.M., 1998. An Introduction to Environmental Biophysics, 2nd edition. Springer.

Chaerle, L., Van Caeneghem, W., Messens, E., Lambers, H., Van Montagu, M., Van Der Straeten, D., 1999. Presymptomatic visualization of plant-virus interactions by thermography. Nat. Biotechnol. 17, 813–816. https://doi.org/10.1038/11765.

Charney, J., Stone, P.H., Quirk, W.J., 1975. Drought in the Sahara: a biogeophysical feedback mechanism. Science 187, 434–435.

Cortes, C., Vapnik, V., 1995. Support-vector networks. Mach. Learn. 20, 273–279.

Cubero-Castan, M., Chanussot, J., Achard, V., Briottet, X., Shimoni, M., 2015. A physics-based unmixing method to estimate subpixel temperatures on mixed pixels. IEEE Trans. Geosci. Remote Sens. 53, 1894–1906. https://doi.org/10.1109/TGRS.2014.2350771.

Damm, A., Paul-Limoges, E., Kükenbrink, D., Bachofen, C., Morsdorf, F., 2020. Remote sensing of forest gas exchange: considerations derived from a tomographic perspective. Glob. Chang. Biol. 26, 2717–2727. https://doi.org/10.1111/gcb.15007.

Davis, K.T., Dobrowski, S.Z., Holden, Z.A., Higuera, P.E., Abatzoglou, J.T., 2019. Microclimatic buffering in forests of the future: the role of local water balance. Ecography 42, 1–11. https://doi.org/10.1111/ecog.03836.

Disney, M.I., Kalogirou, V., Lewis, P., Prieto-Blanco, A., Hancock, S., Pfeifer, M., 2010. Simulating the impact of discrete-return lidar system and survey characteristics over young conifer and broadleaf forests. Remote Sens. Environ. 114, 1546–1560. https://doi.org/10.1016/j.rse.2010.02.009.

Doughty, C.E., Goulden, M.L., 2008. Are tropical forests near a high temperature threshold? J. Geophys. Res. Biogeosci. 114 https://doi.org/10.1029/2007JG000632.

Ellsworth, D.S., Reich, P.B., 1993. Canopy structure and vertical patterns of photosynthesis and related leaf traits in a deciduous forest. Oecologia 96, 169–178.

Exelis Visual Information Solutions, 2015. ENVI v. 5.3. L3 Harris Geospatial, Boulder, CO.

Farquhar, G.D., Sharkey, T.D., 1982. Stomatal conductance and photosynthesis. Annu. Rev. Plant Physiol. 33, 317–345. https://doi.org/10.1146/annurev.pp.33.060182.001533.

Farquhar, G.D., von Caemmerer, S., Berry, J.A., 1980. A biochemical model of photosynthetic CO2 assimilation in leaves of C3 species. Planta 149, 78–90. https://doi.org/10.1007/BF00386231.

Fauset, S., Freitas, H.C., Galbraith, D.R., Sullivan, M.J., Aidar, M.P., Joly, C.A., Phillips, O.L., Vieira, S.A., Gloor, M.U., 2018. Differences in leaf thermoregulation and water use strategies between three co-occurring Atlantic forest tree species. Plant Cell Environ. 41, 1618–1631. https://doi.org/10.1111/pce.13208.

Fisher, J.B., Lee, B., Purdy, A.J., Halverson, G.H., Dohlen, M.B., Cawse-Nicholson, K., Wang, A., Anderson, R.G., Aragon, B., Arain, M.A., Baldocchi, D.D., Baker, J.M., Barral, H., Bernacchi, C.J., Bernhofer, C., Biraud, S.C., Bohrer, G., Brunsell, N., Cappelaere, B., Castro-Contreras, S., Chun, J., Conrad, B.J., Cremonese, E., Demarty, J., Desai, A.R., Ligne, A.D., Foltýnová, L., Goulden, M.L., Griffis, T.J., Grünwald, T., Johnson, M.S., Kang, M., Kelbe, D., Kowalska, N., Lim, J.H., Maïnassara, I., McCabe, M.F., Missik, J.E., Mohanty, B.P., Moore, C.E., Morillas, L., Morrison, R., Munger, J.W., Posse, G., Richardson, A.D., Russell, E.S., Ryu, Y., Sanchez-Azofeifa, A., Schmidt, M., Schwartz, E., Sharp, I., Sigut, L., Tang, Y., Hulley, G., Anderson, M., Hain, C., French, A., Wood, E., Hook, S., 2020. ECOSTRESS: NASA's next generation mission to measure evapotranspiration from the International Space Station. Water Resour. Res. 56 e2019WR026058.

Gates, D.M., Alderfer, R., Taylor, E., 1968. Leaf temperatures of desert plants. Science 159, 994–995.

Gillespie, A.R., Rokugawa, S., Matsunaga, T., Cothern, J.S., Hook, S.J., Kahle, A.B., 1998. A temperature and emissivity separation algorithm for Advanced Spaceborne Thermal Emission and Reflection Radiometer (ASTER) images. IEEE Trans. Geosci. Remote Sens. 36, 1113–1126.

Gray, S.B., Dermody, O., Klein, S.P., Locke, A.M., McGrath, J.M., Paul, R.E., Rosenthal, D.M., Ruiz-Vera, U.M., Siebers, M.H., Strellner, R., Ainsworth, E.A., Bernacchi, C.J., Long, S.P., Ort, D.R., Leakey, A.D., 2016. Intensifying drought eliminates the expected benefits of elevated carbon dioxide for soybean. Nat. Plant 2, 1–8. https://doi.org/10.1038/nplants.2016.132.

Griffin, K.L., Turnbull, M., Murthy, R., 2002. Canopy position affects the temperature response of leaf respiration in *Populus deltoides*. New Phytol. 154, 609–619. https://doi.org/10.1046/j.1469-8137.2002.00410.x.

Gunn, S.R., 1998. Support vector machines for classification and regression. In: University of Southampton Technical Report, pp. 1–54.

Hook, S.J., Cawse-Nicholson, K., Barsi, J., Radocinski, R., Hulley, G.C., Johnson, W.R., Rivera, G., Markham, B., 2020. In-flight validation of the ECOSTRESS, Landsats 7 and 8 thermal infrared spectral channels using the Lake Tahoe CA/NV and Salton Sea CA automated validation sites. IEEE Trans. Geosci. Remote Sens. 58, 1294–1302. https://doi.org/10.1109/TGRS.2019.2945701.

Hulley, G., Freepartner, R., 2019. ECOsystem Spaceborne Thermal Radiometer Experiment on Space Station (ECOSTRESS) Mission: Level 2 Product User Guide v. 2. Jet Propulsion Laboratory, California Institute of Technology.
Hulley, G.C., Hook, S., 2018. ECOsystem Spaceborne Thermal Radiometer Experiment on Space Station (ECOSTRESS): Level-2 Land Surface Temperature and Emissivity Algorithm Theoretical Basis Document (ATBD), 96 pp. Jet Propulsion Laboratory, Pasadena.
Jackson, R., Idso, S., Reginato, R., Pinter, P., 1981. Canopy temperature as a crop water stress indicator. Water Resour. Res. 17, 1133–1138. https://doi.org/10.1029/WR017i004p01133.
Jarvis, P.G., 1995. Scaling processes and problems. Plant Cell Environ. 18, 1079–1089. https://doi.org/10.1111/j.1365-3040.1995.tb00620.x.
Jarvis, P.G., McNaughton, K.G., 1986. Stomatal control of transpiration: scaling up from leaf to region. Adv. Ecol. Res. 15, 1–49.
Johnston, M.R., Andreu, A., Verfaillie, J., Baldocchi, D., Gonzalez-Dugo, M.P., Moorcroft, P.R., 2021. Measuring surface temperatures in a woodland savanna: opportunities and challenges of thermal imaging in an open-canopy ecosystem. Agric. For. Meteorol. 310, 108484. https://doi.org/10.1016/j.agrformet.2021.108484.
Jones, H.G., Sirault, X.R., 2014. Scaling of thermal images at different spatial resolution: the mixed pixel problem. Agronomy 4, 380–396. https://doi.org/10.3390/agronomy4030380.
Kafuti, C., Bourland, N., Mil, T.D., Meeus, S., Rousseau, M., Toirambe, B., Bolaluembe, P. C., Ndjele, L., Beeckman, H., 2020. Foliar and wood traits covary along a vertical gradient within the crown of long-lived light-demanding species of the Congo basin semi-deciduous forest. Forests 11. https://doi.org/10.3390/f11010035.
Khosravipour, A., Skidmore, A.K., Isenburg, M., Wang, T., Hussin, Y.A., 2014. Generating pit-free canopy height models from airborne Lidar. Photogramm. Eng. Remote. Sens. 80, 863–872. https://doi.org/10.14358/PERS.80.9.863.
Kim, Y., Still, C.J., Roberts, D.A., Goulden, M.L., 2018. Thermal infrared imaging of conifer leaf temperatures: comparison to thermocouple measurements and assessment of environmental influences. Agric. For. Meteorol. 248, 361–371. https://doi.org/10.1016/j.agrformet.2017.10.010.
Kobayashi, H., Baldocchi, D.D., Ryu, Y., Chen, Q., Ma, S., Osuna, J.L., Ustin, S.L., 2012. Modeling energy and carbon fluxes in a heterogeneous oak woodland: a three-dimensional approach. Agric. For. Meteorol. 152, 83–100. https://doi.org/10.1016/j.agrformet.2011.09.008.
Kuhn, M., 2019. caret: Classification and regression training. In: R Package Version 6.0-84, with Contributions from J. Wing, S. Weston, A. Williams, C. Keefer, A. Engelhardt, T. Cooper, Z. Mayer, B. Kenkel, M. Benesty. R. Lescarbeau, A. Ziem, L. Scrucca, Y. Tang, C. Candan, T. Hunt, and the R Core Team.
Laben, C.A., Brower, B.V., 2000. Process for enhancing the spatial resolution of multispectral imagery using pan-sharpening. United States Patent 6,011,875.
Lange, O., Losch, R., Schulze, E.D., Kappen, L., 1971. Responses of stomata to changes in humidity. Planta 100, 76–86.
Lapidot, O., Ignat, T., Rud, R., Rog, I., Alchanatis, V., Klein, T., 2019. Use of thermal imaging to detect evaporative cooling in coniferous and broadleaved tree species of the mediterranean maquis. Agric. For. Meteorol. 271, 285–294. https://doi.org/10.1016/j.agrformet.2019.02.014.
Maguire, A.J., Eitel, J.U., Griffin, K.L., Magney, T.S., Long, R.A., Vierling, L.A., Schmiege, S.C., Jennewein, J.S., Weygint, W.A., Boelman, N.T., Bruner, S.G., 2020. On the functional relationship between fluorescence and photochemical yields in complex evergreen needleleaf canopies. Geophys. Res. Lett. 47, 1–9. https://doi.org/10.1029/2020GL087858.
Malakar, N.K., Hulley, G.C., Hook, S.J., Laraby, K., Cook, M., Schott, J.R., 2018. An operational land surface temperature product for Landsat thermal data: methodology and validation. IEEE Trans. Geosci. Remote Sens. 56, 5717–5735. https://doi.org/10.1109/TGRS.2018.2824828.
Marrs, J.K., Reblin, J.S., Logan, B.A., Allen, D.W., Reinmann, A.B., Bombard, D.M., Tabachnik, D., Hutyra, L.R., 2020. Solar-induced fluorescence does not track photosynthetic carbon assimilation following induced stomatal closure. Geophys. Res. Lett. 47, 1–11. https://doi.org/10.1029/2020GL087956.
Martin, T.A., Hinkley, T.M., Meinzer, F.C., Sprugel, D.G., 1999. Boundary layer conductance, leaf temperature and transpiration of abies amabilis branches. Tree Physiol. 19, 435–443.
Maurer, T., 2013. Hot to pan-sharpen images using the gram-schmidt pan-sharpen method – a recipe. In: International Archives of the Photogrammetry, Remote Sensing and Spatial Information Sciences XL-1/W1, pp. 239–244.
McAllister, S., Grenfell, I., Hadlow, A., Jolly, W.M., Finney, M., Cohen, J., 2012. Piloted ignition of live forest fuels. Fire Saf. J. 51, 133–142. https://doi.org/10.1016/j.firesaf.2012.04.001.
McGregor, I.R., Helcoski, R., Kunert, N., Tepley, A.J., Gonzalez-Akre, E.B., Herrmann, V., Zailaa, J., Stovall, A.E.L., Bourg, N.A., McShea, W.J., Pederson, N., Sack, L., Anderson-Teixeira, K.J., 2020. Tree height and leaf drought tolerance traits shape growth responses across droughts in a temperate broadleaf forest. New Phytol. https://doi.org/10.1111/nph.16996.
Medina, E., Sobrado, M., Herrera, R., 1978. Significance of leaf orientation for leaf temperature in an amazonian sclerophyll vegetation. Radiat. Environ. Biophys. 15, 131–140. https://doi.org/10.1007/BF01323262.
Meerdink, S.K., Hook, S.J., Roberts, D.A., Abbott, E.A., 2019. The ECOSTRESS spectral library version 1.0. Remote Sens. Environ. 230, 1–8. https://doi.org/10.1016/j.rse.2019.05.015.
Michaletz, S.T., 2018. Evaluating the kinetic basis of plant growth from organs to ecosystems. New Phytol. 219, 37–44. https://doi.org/10.1111/nph.15015.
Miller, B.D., Carter, K.R., Reed, S.C., Wood, T.E., Cavaleri, M.A., 2021. Only sun-lit leaves of the uppermost canopy exceed both air temperature and photosynthetic thermal optima in a wet tropical forest. Agric. For. Meteorol. 301-302, 108347. https://doi.org/10.1016/j.agrformet.2021.108347.
Monson, R., Baldocchi, D., 2014. Terrestrial Biosphere-Atmospjere Fluxes, 1st edition. Cambridge University Press.
Pau, S., Detto, M., Kim, Y., Still, C.J., 2018. Tropical forest temperature thresholds for gross primary productivity. Ecosphere 9, e023111. https://doi.org/10.1002/ecs2.2311.
R Core Team, 2020. R: A Language and Environment for Statistical Computing. R Foundation for Statistical Computing, Vienna, Austria.
Raschke, K., 1960. Heat transfer between the plant and the environment. Annu. Rev. Plant Physiol. 11, 111–126. https://doi.org/10.1146/annurev.pp.11.060160.000551.
Renaud, V., Innes, J.L., Dobbertin, M., Rebetez, M., 2011. Comparison between open-site and below-canopy climatic conditions in Switzerland for different types of forests over 10 years (1998-2007). Theor. Appl. Climatol. 105, 119–127. https://doi.org/10.1007/s00704-010-0361-0.
Rey-Sánchez, A.C., Slot, M., Posada, J.M., Kitajima, K., 2016. Spatial and seasonal variation in leaf temperature within the canopy of a tropical forest. Clim. Res. 71, 75–89. https://doi.org/10.3354/cr01427.
Richardson, A.D., Aubrecht, D.M., Basler, D., Hufkens, K., Muir, C.D., Hanssen, L., 2020. Developmental changes in the reflectance spectra of temperate deciduous tree leaves and implications for thermal emissivity and leaf temperature. New Phytol. 229, 791–804. https://doi.org/10.1111/nph.16909.
Rollinson, C.R., Alexander, M.R., Dye, A.W., Moore, D.J., Pederson, N., Trouet, V., 2020. Climate sensitivity of understory trees differs from overstory trees in temperate mesic forests. Ecology. https://doi.org/10.1002/ecy.3264.
Rotenberg, E., Yakir, D., 2011. Distinct patterns of changes in surface energy budget associated with forestation in the semiarid region. Glob. Chang. Biol. 17, 1536–1548. https://doi.org/10.1111/j.1365-2486.2010.02320.x.
Roussel, J.R., Auty, D., 2020. lidR: Airborne LiDAR Data Manipulation and Visualization for Forestry Applications. R Package Version 3.0.4.
Rubio, E., Caselles, V., Badenas, C., 1997. Emissivity measurements of several soils and vegetation types in the 8-14 μm wave band: analysis of two field methods. Remote Sens. Environ. 59, 490–521. https://doi.org/10.1016/S0034-4257(96)00123-X.
Rubio, E., Caselles, V., Coll, C., Valour, E., Sospedra, F., 2003. Thermal-infrared emissivities of natural surfaces: improvements on the experimental set-up and new measurements. Int. J. Remote Sens. 24, 5379–5390. https://doi.org/10.1080/0143116031000102412.
Ryu, Y., Verfaillie, J., Macfarlane, C., Kobayashi, H., Sonnentag, O., Vargas, R., Ma, S., Baldocchi, D.D., 2012. Continuous observation of tree leaf area index at ecosystem scale using upward-pointing digital cameras. Remote Sens. Environ. 126, 116–125. https://doi.org/10.1016/j.rse.2012.08.027.
Sage, R.F., Kubien, D.S., 2007. The temperature response of C3 and C4 photosynthesis. Plant Cell Environ. 30, 1086–1106. https://doi.org/10.1111/j.1365-3040.2007.01682.x.
Scherrer, D., Bader, M.K.F., Körner, C., 2011. Drought-sensitivity ranking of deciduous tree species based on thermal imaging of forest canopies. Agric. For. Meteorol. 151, 1632–1640. https://doi.org/10.1016/j.agrformet.2011.06.019.
Shukla, J., Mintz, Y., 1982. Influence of land-surface evapotranspiration on the earth's climate. Science 215, 1498–1501.
Silvestri, M., Romaniello, V., Hook, S., Musacchio, M., Teggi, S., Buongiorno, M.F., 2020. First comparisons of surface temperature estimations between ecostress, aster and landsat 8 over italian volcanic and geothermal areas. Remote Sens. 12 https://doi.org/10.3390/RS12010184.
Sinoquet, H., Roux, X.L., Adam, B., Ameglio, T., Daudet, F.A., 2001. RATP: a model for simulating the spatial distribution of radiation absorption, transpiration and photosynthesis within canopies: application to an isolated tree crown. Plant Cell Environ. 24, 395–406.
Slot, M., Winter, K., 2017. In situ temperature relationships of biochemical and stomatal controls of photosynthesis in four lowland tropical tree species. Plant Cell Environ. 40, 3055–3068. https://doi.org/10.1111/pce.13071.
Smith, N.G., Dukes, J.S., 2017. Short-term acclimation to warmer temperatures accelerates leaf carbon exchange processes across plant types. Glob. Chang. Biol. 23, 4840–4853. https://doi.org/10.1111/gcb.13735.
Smith, W.K., Nobel, P.S., 1977. Temperature and water relations for sun and shade leaves of a desert broadleaf, hyptis emoryi. Source. J. Exp. Bot. 28, 169–183.
Still, C., Powell, R., Aubrecht, D., Kim, Y., Helliker, B., Roberts, D., Richardson, A., Goulden, M., 2019. Thermal imaging in plant and ecosystem ecology: applications and challenges. Ecosphere 10, e02768. https://doi.org/10.1002/ecs2.2768.
Still, C.J., Rastogi, B., Page, G.F.M., Griffith, D.M., Sibley, A., Schulze, M., Hawkins, L., Pau, S., Detto, M., Helliker, B.R., 2021. Imaging canopy temperatures: shedding (thermal) light on ecosystem processes. New Phytol. 230, 1746–1753. https://doi.org/10.1111/nph.17321.
Taiz, L., Zeiger, E., 2002. Plant Physiology, 3rd edition. Sinauer Associates, Inc.
Wang, H., Atkin, O.K., Keenan, T.F., Smith, N.G., Wright, I.J., Bloomfield, K.J., Kattge, J., Reich, P.B., Prentice, I.C., 2020. Acclimation of leaf respiration consistent with optimal photosynthetic capacity. Glob. Chang. Biol. 26, 2573–2583. https://doi.org/10.1111/gcb.14980.

Wilson, C., Grace, J., Allen, S., Slack, F., 1987. Temperature and stature: a study of temperatures in montane vegetation. Funct. Ecol. 1, 405–413. https://doi.org/10.2307/2389798.

Woods, H.A., Saudreau, M., Pincebourde, S., 2018. Structure is more important than physiology for estimating intracanopy distributions of leaf temperatures. Ecol. Evol. 8, 5206–5218. https://doi.org/10.1002/ece3.4046.

Xue, J., Anderson, M.C., Gao, F., Hain, C., Sun, L., Yang, Y., Knipper, K.R., Kustas, W.P., Torres-Rua, A., Schull, M., 2020. Sharpening ECOSTRESS and VIIRS land surface temperature using harmonized Landsat-Sentinel surface reflectances. Remote Sens. Environ. 251, 112055. https://doi.org/10.1016/j.rse.2020.112055.